Experimental Evaluation of the Feasibility of Wearable Piezoelectric Energy Harvesting

by

Shiva Bandyopadhyay

A Thesis Presented in Partial Fulfillment
of the Requirement for the Degree
Master of Science

Approved July 2020 by the
Graduate Supervisory Committee:

Umit Ogras, Chair
Deliang Fan
Georgios Trichopoulos

ARIZONA STATE UNIVERSITY

August 2020

ABSTRACT

Technological advances in low power wearable electronics and energy optimization techniques make motion energy harvesting a viable energy source. However, it has not been widely adopted due to bulky energy harvester designs that are uncomfortable to wear. This work addresses this problem by analyzing the feasibility of powering low wearable power devices using piezoelectric energy generated at the human knee. We start with a novel mathematical model for estimating the power generated from human knee joint movements. This thesis's major contribution is to analyze the feasibility of human motion energy harvesting and validating this analytical model using a commercially available piezoelectric module. To this end, we implemented an experimental setup that replicates a human knee. Then, we performed experiments at different excitation frequencies and amplitudes with two commercially available Macro Fiber Composite (MFC) modules. These experimental results are used to validate the analytical model and predict the energy harvested as a function of the number of steps taken in a day. The model estimates that 13μW can be generated on an average while walking with a 4.8% modeling error. The obtained results show that piezoelectricity is indeed a viable approach for powering low-power wearable devices.

Dedicated to my family

ACKNOWLEDGMENTS

This thesis represents a step towards the goal of developing a Human Motion Energy Harvesting System for the battery-free operation of low-power wearable devices which will be helpful towards a wide range of applications for the betterment of humanity. There have been several people who have directly or indirectly contributed to this work.

My deepest gratitude goes to my advisor, Dr. Umit Ogras, for the patience, advice and guidance he offered me throughout the last year. This thesis would not be possible without his support. I would also like to thank Dr. Deliang Fan and Dr. Georgios C. Trichopoulos for taking the time out from their busy schedule to be part of my thesis defense committee.

I would also like to extend my deep gratitude to Yigit Tuncel for his immense help with the construction of this work. I would like to thank Shambhavi Vikram Kulshrestha for her support and immense help in performing experiments. I would like to thank Audrey Mendez for her timely help with creating a new experimental setup. I thank Ganapati Bhat, Sizhe An, Gokul Krishna, Toygun Basaklar and Shruti Yadav, Sumit Mandal, and Anish N. K for their feedback with my work.

My parents Dr. G G Bandyopadhyay and Mrs. Archana Bandyopadhyay, my sister Ankusha, and girlfriend Preeti deserve utmost gratitude for this work. Their love, endless support and understanding from thousands of miles away have been my source of inspiration.

My Master's term at Arizona State University provided an environment that made my studies engaging, enjoyable, profitable and productive. I would like to thank all who were involved. I thank Dr. Chaitali Chakrabarti and Dr. Sule Ozev for providing financial support and giving me the opportunity to be a Teaching Assistant in their course on Digital Systems and Circuits. I want to especially thank Dr. Umit Ogras for letting me be a part of his wonderful team and supporting me throughout my research in every way.

TABLE OF CONTENTS

CHAPTER Page

LIST OF TABLES

LIST OF FIGURES

Figure Page

Chapter 1

INTRODUCTION

Recent advances in low-power electronics, energy management techniques, and technology node scaling have enabled transformational changes in various domains. One such field that has significantly benefited from these advances is wearable electronics and applications [34, 7, 30]. However, the limited battery capacity of such wearable devices has hindered their widespread adoption. This challenge has motivated research to enable wearable energy harvesting as an alternative energy source. With energy harvesting, the device can generate usable electrical energy from various sources in the user's environment [44, 52].

Energy harvesting is the collection of energy present in the environment. The most common energy sources for wearable energy harvesting are light, motion, electromagnetic waves, and heat [57, 46, 42, 37]. Motion energy is particularly interesting as it has usable harvesting potential [21] and is available on demand. For example, studies show that close to 1W can be harvested from human knee while walking. Moreover, this energy is available when required by wearable activity monitoring applications. Therefore, motion energy harvesting is an ideal energy source in such wearable applications.

Motion energy harvesting solutions commonly use piezoelectric materials to transform mechanical energy to electrical potential difference [55]. The piezoelectric effect generates electric charge on two opposite sides of a piezoelectric crystal when it is subjected to

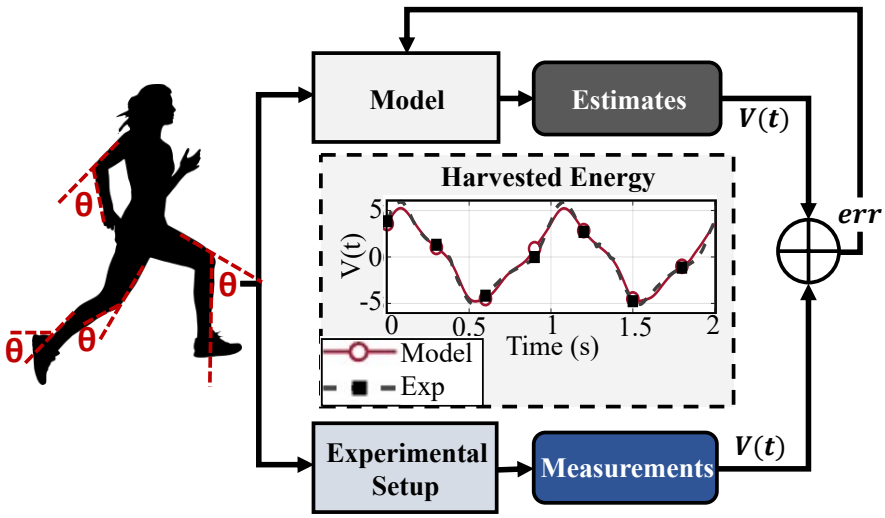

Figure 1.1: Overview of model and experimental validation of piezoelectrictric energy harvesting from human joint bending [58]

mechanical stress. Consequently, the accumulation of charge creates an electrical potential difference. This electric charge is harvested and stored for later use.

1.1 Limitations in Current Technologies

Energy harvesting from vibration sources typically uses piezoelectric energy harvesting, as shown in the literature [60, 39, 59]. These vibrations often have high frequencies in the order or 100 or 1000 Hz, which is much higher than those of human gait movements during walking and running. However, piezoelectric materials generate maximum power at mechanical resonant frequencies, which are similar to these vibrations. Furthermore, these materials have historically been inflexible and brittle [39]. Such issues limited the use of piezoelectric materials in wearable applications. Studies in wearable piezoelectric energy harvesting (PEH) literature address these challenges by employing frequency up/down-conversion techniques through intricate mechanical designs [47] to match the frequency of the mechanical forces from human motion to the resonant frequency of the used piezoelectric beam.

However, these intricate mechanical designs are typically placed in an external frame worn by the user, making such designs bulky and inflexible, thus preventing these approaches from being *truly wearable*.

In summary, the prior approaches are not suitable for wearable applications due to two main reasons.

- Their inflexibility, size and weight limits their use in wearable applications.
- Their resonant frequencies are in the order of 100 or 1000s of Hz, which is orders of magnitudes larger than that of human motion.

Flexible piezoelectric materials, such as polyvinylidene fluoride (PVDF) resolved the fallacies due to bulkiness and inflexibility and enabled the placement of piezoelectric materials directly on the joints [48]. For example, knees, elbows, and ankles are potentially apt places for placing these materials as depicted in Fig. 1.1 because they undergo considerable bending and hence produce significant bending on a coupled piezoelectric energy harvester. So, there is a strong need for the piezoelectric energy harvester to be flexible and harvest energy at *low-frequency and large-bending* motions. While this approach removes the wearability and flexibility concerns, it increases the risk of insufficient energy output.

1.2 Overview of the Proposed Approach

We consider a flexible piezoelectric patch directly placed on one of the joints, such as those shown in Fig. 1.1. The proposed approach consists of three major components, as illustrated in Fig. 1.3: 1) Modeling the physical displacement during *large-bending conditions*. 2) Converting the physical movement to electrical voltage. This approach is published in ACM/IEEE International Symposium on Low Power Electronics and Design (ISLPED), 2020 [58]. 3) Experimental validation and parameter identification for the proposed model.

1. The joint bending model relates the joint bending angle to strain induced in the piezoelectric patch. It calculates horizontal and vertical displacements and the curvature of the piezoelectric patch for a given joint movement. Then, using these, it calculates the strain in the piezoelectric patch, as explained in section 3.1.1. This sub-model addresses the strain calculation in a large-bending scenario introduced by large joint rotations.

2. The piezoelectricity model expresses the generated voltage according to the induced strain in the piezoelectric material. Firstly, it calculates the accumulated charge in the material and then, The time derivative of charge yields the current passing through the piezoelectric patch. Finally, the current through the load resistance determines the voltage across this load and generated power, as explained in section 3.1.2.

3. Experimental validation is crucial to demonstrate the practical use of the proposed model and identify the values of model parameters with significant uncertainty. In this part of the study, we consider a piezoelectric patch directly placed on the front of the human knee, since this position has the most abundant energy harvesting potential [21]. Obtaining reliable measurements from the human knee is challenging due to errors caused by the knee's nonuniform surface and human errors. Also, repeatability of the results with real subjects is another challenge, due to the fact that the amplitude and frequency of human motion are uncontrollable.

Figure 1.2: Macro Fiber Composite (MFC Patch), MFC8528P2 [56]

To obtain reliable and repeatable measurements and overcome these challenges, we removed the human factor by designing a 3D printed mechanical bending frame. This mechanical frame is used to record the generated voltages from two Macro Fiber Composite (MFC) piezoelectric patches with different dimensions under sinusoidal actuation with different motion frequencies and amplitudes.

Finally, the model is further optimized to minimize the error between experimental and modeling results by tuning critical parameters in the model, as illustrated in Fig. 1.1. Experimental evaluation and real-life application scenarios are presented in Section 4.3.

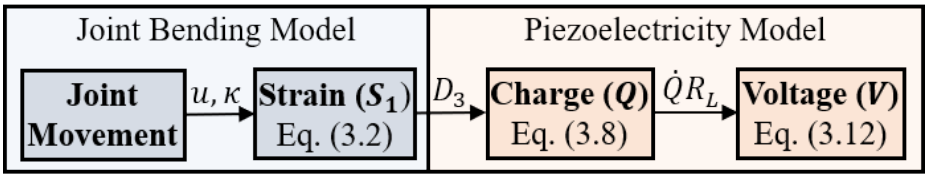

Figure 1.3: Overview of the proposed modeling approach.u: Horizontal Displacement. κ: Curvature. D_1: Electric Displacement. R: Load resistance.

1.3 Key Contributions

The contributions of this work are as follows. First, we describe the mathematical model for the energy harvesting output of a piezoelectric patch directly placed on a human knee joint [58]. Then, we describe an experimental setup that imitates a human knee joint and provides an extensive experimental evaluation that validates the model and demonstrates the energy harvesting potential of wearable piezoelectric energy harvesting.

Using the mathematical model, we show that wearable piezoelectric energy harvesting potential from the knee joint is sufficient to sustain low-power applications. According to our results, users can generate, on average, 13 μW power while walking. Our evaluations also show that the monthly energy capacity of a person taking 7500 steps/day is equivalent to a 0.34 mAh battery rated at 1.2V.

In short, the major contributions of this work are as follows:

- A novel experimental setup for human motion energy harvesting using piezoelectric patches mounted on a joint.
- An experimental data set using the novel experimental setup.
- An experimental evaluation that validates a mathematical model that demonstrates the potential of wearable piezoelectric energy harvesting.

A condensed version of this work is presented in ACM/IEEE in ISLPED, 2020 [58] and the ISLPED Design Contest.

1.4 Thesis Organization

The rest of this thesis is organized as follows. Chapter 2, discusses the related work on different energy harvesting methods, with a primary focus on energy harvesting from human motion. Chapter 3, starts with a discussion of the theory behind the piezoelectric effect and then proceeds with a large bending mathematical model for a flexible piezoelectric energy harvester mounted on a human knee. Chapter 4, shows the feasibility of using a piezoelectric energy harvester mounted on a human knee with the initial experiments performed using two different commercially available piezoelectric energy harvesters and describe the design of a new experimental setup, which mimics a human knee. Then, it discusses the experimental methodology and shows that the experimental results agree with the mathematical model—furthermore, the relation between the model and actual human walking. It provides power generation estimates and compares them with the power consumption of some low power wearable applications to show that this is a feasible way to power wearable devices. A commercially available piezoelectric energy harvesting circuit is used to harvest energy, thereby demonstrating the practicability of human motion energy

harvesting. Additionally, We then proceed to provide insights on the run-time use of this model. Finally, chapter 5 sums up this work and points direction for future work.

Chapter 2

RELATED WORK

Recent advances in low power technology have made wearable devices and applications easily accessible and explode in popularity. Researchers have demonstrated various wearable applications operating in the sub-mW power range [65, 64, 43, 45, 12]. For example, Kang et al. present a face frontalization processor for face recognition with a power consumption of 0.53mW [32]. Another recent work introduces a low power Bluetooth flexible emotion sensor [36].

An important application area of low-power wearable devices is human health and activity monitoring [13]. Especially, physically stretchable and flexible wearable devices can enable electronic patches for a wide range of novel applications [6, 62, 41, 27, 14]. A low power wearable device is presented in [2]. The authors achieve a low power system that consumes 172μW on the ASIC for heart rate extraction from the raw signal, with the entire system consuming 1.66mW power. As the technology nodes become smaller and smaller, sub 50μW applications are becoming more viable. One such state of the art application is presented in [49]. The authors introduce a test SoC on the 28nm CMOS process node, specifically for wearable and IoT applications. While the SoC integrates an ARM-based processor, DSP, and hardware accelerators for computer vision, it consumes less than 9μW per MHz. Similarly, a low-power hardware accelerator for human activity recognition is presented in [16]. A similar, much specific low-cost asynchronous SoC for ECG applications is presented in [67], which consumes 3μW, does not require clock generators and off-chip antennas, thereby, making it a good option for disposable wireless ECG patches.

Energy harvesting from mechanical sources has existed for a considerable amount of time. Turbines, dynamos, and such devices are typical examples of mechanical to electrical

transducers. Approaches for powering devices using vibration energy harvesting are also common and, as such, have been used in structural monitoring for bridges, tunnels, and windmills [40, 17, 5]. Energy harvesting can enable self-powered devices when combined with dynamic energy allocation and optimization techniques [15, 11].

There have been many studies on human motion energy harvesting. Various approaches include electromagnetic, temperature gradient, electro-mechanical, and piezoelectric. In one such study, [25], researchers have demonstrated the potential of a looped inertial energy harvester, which consists of a metal ball that moves freely inside a loop and induces a current in the coils. Another study explores the possibility of harvesting energy from the waste thermal energy of the human body. They place thermoelectric modules on various parts of the body to harvest a total boosted power of 24.7μW [63]. In [26], they demonstrate a electromagnetic energy harvester with a energy density of 730μWcm^{-3}. Another study explores the possibility of a knee mounted electro-mechanical device [20], which intends to powering prosthetic limbs. They demonstrate the device's design, which mounts on the side of the user's knee.

Researchers have demonstrated the potential of piezoelectric energy harvesting from various parts of the human body. [50, 51] demonstrate the design and optimization of a lead zirconate titanate (PZT) based piezoelectric energy harvester mounted within the user's footwear. Another work [28] explores the possibility of a hybrid energy harvesting system by combining a piezoelectric and electromagnetic energy harvesting and claims that the combined topology enhances power output and DC stability. Furthermore, [38] shows a PZT-microelectromechanical system (MEMS) -based energy harvester with a low resonant frequency of 36Hz with a wide band operation frequency of 17Hz. They further show that the harvester's wideband operation increased the voltage and power levels of the harvester. A low-frequency energy harvester with a permanent magnet, a proof mass,

and an Magnetic Shape Memory Alloy-Macro Fiber Composite (MSMA-MFC) laminate composite, which generates 0.53μW at 19Hz, is explored in [31].

Piezoelectric energy harvesters (PEHs) have resonant frequencies, far more than human motion. It is shown that frequency up-conversion is a viable approach to harvest energy. A study uses a cantilever beam with a piezoelectric patch attached to the end of it mounted on the human leg for frequency up-conversion. Even though the power generated was close to 2.8mW, this method is very bulky, hence impractical as a wearable device. [29]. Another study involving a linear kinetic energy harvester [4] explores a cantilever based PEH mounted on the human arm. They claim an RMS power of 50 μW from regular human activities and compare them with nonlinear designs. However, this design also proves to be bulky, and it restricts free motion due to its inflexibility and hence, impractical for use in the real world as a wearable device. [53] shows a similar effort to harvest energy using piezoelectricity. They present an impact-driven piezoelectric energy harvester from human motion. The design involves a high-frequency PZT-5A bimorph cantilever beam with a proof mass at one end placed inside an aluminum casing. The device was attached to the leg of a test subject. They were able to harvest 51 μW with fast walking activity. Even though the results seem positive, the fact that the devices protrude from the user's leg is discomfort and, at times, even impractical. As we can see, a considerably low effort has been put on harvesting energy from highly flexible materials placed directly on joints, which make human motion energy harvesting practical and comfortable for the user. Another approach presented by [61] involves constructing a device mounted on the human leg using PZT, steel plates, and magnets to capture the human leg's swinging motion. Even though the design to be very bulky, the harvested power is about 16μW.

The lack of comfort due to the bulkiness and impracticability of current approaches to human motion energy harvesters motivated us to use novel flexible piezoelectric materials directly coupled with body joints. One such potential flexible PEH called Macro Fiber

Table 2.1: A compilation of recent related work in wearable piezoelectric energy harvesting

Ref	Analytical Model	Experimental Validation	Large Bending	Flexible Form-factor	Reported Power
[35]	✓	✓	✗	✗	6 mW
[48]	✗	✓	✓	✓	1.9 μW
[9]	✗	✓	✓	✓	1.0 μW
[18]	✓	✗	✗	✓	1.0 μW
[53]	✗	✓	✗	✗	51.0 μW
[29]	✓	✓	✗	✗	2.8 mW
[61]	✓	✓	✗	✗	16.4 μW
This Work	✓	✓	✓	✓	**13 μW**

Composite (MFC) [56] is analyzed in [22]. They have analyzed the effect of uniform physical strain on MFC using a test setup and claim that they are fail-proof for more than 10^{10} cycles. Researchers demonstrated the potential of using flexible piezoelectric materials directly coupled to movements of the joints in the body [48, 9]. In one such work, researchers placed polyvinylidene difluoride (PVDF) and MFC beams at various locations on the human body [48, 8]. They recorded the harvested energy at these different locations during different physical activities, such as walking, jogging, and climbing up/downstairs. They observed an increase in energy output with higher frequency motion compared to a lower frequency one. They reported 1.9μW during walking and 3.7μW during jogging. A theoretical analysis of the power generated using a PVDF patch mounted on a human knee using a small angle approximation is provided in [19]. However, such an approximation is inadequate as human knee motion involves large angular movements. In another study, researchers built a human knee inspired mechanical frame to explore the dynamics of the energy harvesting from human gait [9]. They investigated the dependence of energy on

the frequency and amplitude of the motion and claimed that the harvested energy increases with both variables. They reported results by extracting knee angle data from a motion capture data set and feeding it to their framework. According to those results, close to 1W is generated from a knee harvester during the walking motion. Despite the previous effort on analyzing the energy dependence on the underlying motion, neither of these studies characterized the energy generation in terms of the parameters in the whole system and then proved using experimental validation.

Chapter 3

MODELLING AND ANALYSIS

3.1 Modeling of Piezoelectric Energy Harvesting from Joint Movement

A mathematical model was developed at eLab to explore piezoelectric power generated from flexible piezoelectric patches mounted on human joints. In most piezoelectricity literature, the electrical forces induced by the piezoelectric material are comparable to the mechanical forces such as vibration. These electrical forces are taken into consideration through the mechanical governing equation. In our case, however, the mechanical forces acting on the piezoelectric patch due to large-bending motion are much larger than the generated electrical forces, allowing the electrical and mechanical domains to be decoupled entirely [23]. Hence, we consider only the electrical governing equation in this study [24]:

$$D_1 = \epsilon_{33}^S E^S + e_{31} S_1 \tag{3.1}$$

where D_1 is the electric displacement field, ϵ_{33}^S is the permitivity under constant strain, E^S is the electric field between the electrodes of the piezoelectric sensor, e_{31}=$Y_p d_{31}$ is the piezoelectric constant for the bending mode and S_1 is the strain induced in the piezoelectric material due to bending.

The input to the system is the strain S_1 in the piezoelectric material. The following mechanical joint bending model is used to obtain the strain as a function of the joint angle:

3.1.1 Mechanical Joint Bending Model

We use a large bending representation of a beam attached directly to the human knee, as shown in Fig. 3.1. Here, the joint is modeled as a circular profile with a radius ρ. The

Table 3.1: Summary of symbols used in this work

Symbol	Parameter	Symbol	Parameter
D_1	Electric displacement field	ϵ_{33}^S	Permittivity under constant strain
V	Generated voltage	Q	Accumulated charge
i	Generated current	A	PZ Area
E^S	Electric field	L	PZ Length
S_1	Strain	W	PZ Width
κ	Curvature	C	PZ Capacitance
u	Horz. displacement	R	PZ Load
d_{31}	Strain coefficient	Y_p	PZ Young's Modulus
θ	Joint bend angle	h_p	PZ Thickness
ω	Vert. displacement	Y_s	SB Young's Modulus
r	Radius of curvature	h_s	SB Thickness
e_{31}	Electromechanical coupling coefficient [23]	h_{pc}	Distance to neutral axis

PZ: Piezoelectric Patch. SB: Substrate.

piezoelectric patch bends along this circular profile following the joint bend angle Θ. The neutral position of the patch is shown with ①. As joint bends, the patch goes from position ① to ②.

The point s=0 corresponds to the clamped end of the patch. The point, s=s_0 corresponds to the first point in contact with the circular profile, and the point s=s_1 corresponds to the last point in contact with the circular profile. The point s=L is the free end of the patch. Therefore, using the arc length relation, we express the length of bent piezoelectric material as s_1=$s_0 + \rho\theta(t)$.

As the piezoelectric patch bends along the circular profile, the points on it exhibit horizontal and vertical displacements u(s,t) and ω(s,t). In a large bending scenario, the strain is a function of both of these quantities [23]:

$$S_1(s,t) = h_{pc}\frac{\frac{\partial^2\omega}{\partial s^2}}{\left(1+(\frac{\partial\omega}{\partial s})^2\right)^{\frac{3}{2}}} + \frac{\partial u}{\partial s} \tag{3.2}$$

where h_{pc}=$\frac{Y_s h_s(h_p+h_s)}{2(Y_p h_p+Y_s h_s)}$ is the distance to the neutral axis in the thickness direction [24, 23]. The term next to h_{pc} is the curvature $\kappa(s,t)$ of the patch and due to the circular profile of the joint, it reduces to

$$\kappa(s,t) = \begin{cases} 0, & 0 \le s \le s_0 \\ \frac{1}{\rho}, & s_0 \le s \le s_1 \\ 0, & s_1 \le s \le L \end{cases} \tag{3.3}$$

Where ρ is the radius of curvature.

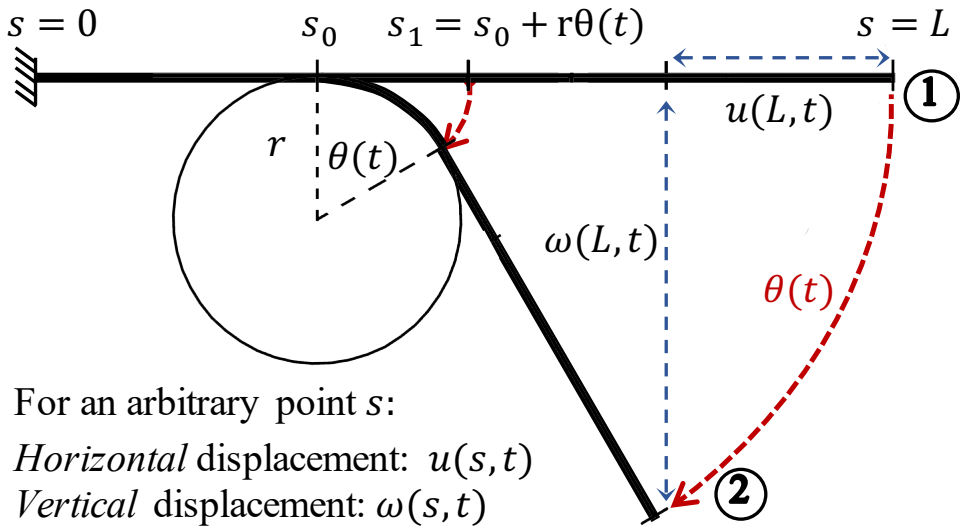

Figure 3.1: Bending model of a piezoelectric patch placed on the human knee.

Finally, we formulate the expression for the horizontal displacement as follows:

$$u(s,t) = \begin{cases} 0, & 0 \leq s \leq s_0 \\ s_0 + \rho sin\theta(t) - s, & s_0 \leq s \leq s_1 \\ s_0 + \rho sin\theta(t) + & \\ (L - (s_0 + \rho\theta(t)))\, cos\theta(t) - s, & s_1 \leq s \leq L \end{cases} \tag{3.4}$$

Next, we develop the piezoelectricity model to obtain the accumulated charge due to the induced strain in the piezoelectric material.

3.1.2 Piezoelectricity Model

Applying the Gauss Law to equation 3.1, we obtain the accumulated charge as follows:

$$Q = \int_A D_1 dA = \int_A \left(\epsilon_{33}^S E^S + e_{31} S_1\right) dA \tag{3.5}$$

Substituting equation 3.2 for S_1 and E^S=$\frac{V}{h_p}$ where V is the voltage and h_p is the thickness of the piezoelectric material, an then evaluating the integral assuming V is constant along the whole area, and S_1 only changes along the length of the patch, we obtain:

$$Q = \frac{\epsilon_{33}^S WL}{h_p} V + e_{31} W \int_0^L \left(h_{pc}\kappa(s,t) + \frac{\partial u(s,t)}{\partial s} \right) ds \tag{3.6}$$

Here W and L denote the width and length of the piezoelectric patch, respectively. The term $\frac{\epsilon_{33}^S WL}{h_p}$ is referred to as the capacitance of the patch [24], and is denoted by C from hereon. The integral in (3.6), is evaluated by dividing the first term into three regions along the length of the patch, and the second term is readily integrable:

$$\begin{aligned} &\int_0^L \left(h_{pc}\kappa(s,t) + \frac{\partial u(s,t)}{\partial s} \right) ds = \\ &\int_0^{s_0} \left(h_{pc}\kappa(s,t)\right) ds + \int_{s_0}^{s_1} \left(h_{pc}\kappa(s,t)\right) ds + \\ &\int_{s_1}^{L} \left(h_{pc}\kappa(s,t)\right) ds + \left(u(L,t) - u(0,t)\right) \end{aligned} \tag{3.7}$$

With (3.3) and (3.4) plugged into (3.7), it reduces to

$$Q(t) = CV(t) + e_{31}W\left(h_{pc}\theta(t) + u(L,t)\right) \tag{3.8}$$

Next, we take the time derivative of $Q(t)$ to obtain the electrical current generated by the piezoelectric patch. In what follows, $\dot{x}$ is used to denote $\frac{dx}{dt}$.

$$i = \frac{V}{R} = C\dot{V} + e_{31}W\left(h_{pc}\dot{\theta} + \dot{u}[L]\right) \tag{3.9}$$

Here, R denotes the load impedance connected between the electrodes of the piezoelectric patch. Manipulating the expression to obtain the form of a ordinary differential equation, we get:

$$\dot{V} = \frac{-1}{RC}V + \frac{e_{31}W}{C}\left(h_{pc}\dot{\theta} + \dot{u}[L]\right) \tag{3.10}$$

We obtain $\dot{u}[L]$ from (3.4) as:

$$\dot{u}[L] = sin\theta\left(s_0 + \rho\theta - L\right)\dot{\theta} \tag{3.11}$$

and plug it in (3.10). Therefore, piezoelectric voltage is governed by the following equation:

$$\dot{V} = \frac{-1}{RC}V + \frac{e_{31}W}{C}\left(h_{pc}\dot{\theta} + sin\theta(s_0 + \rho\theta - L)\dot{\theta}\right) \tag{3.12}$$

To compensate for the deviations of parameters from their datasheet values and errors due to experimental measurements, we introduce fitting parameters p, q_1 and q_2 and bring the equation to the following form:

$$\dot{V} = \frac{-1}{RC}V + \frac{B}{C}\left(h_{pc}U_1 p + U_2(\frac{q_1}{R} + q_2)\right) \tag{3.13}$$

where $B = e_{31}W$, $U_1 = \dot{\theta}$, $U_2 = sin\theta(s_0 + \rho\theta - L)\dot{\theta}$.

In small-bending problems, typically $q_1, q_2 = 0$ and $p = 1$ as horizontal displacement is negligible compared to the length of the patch and all the contribution is from U_1. However, in the large-bending problem at hand, both U_1 and U_2 contribute to the voltage.

Equation 3.13 is solved by the *ode45* solver in MATLAB. The solution is calculated from $t = 0$ to $t = 10$ seconds with $V_0 = 0$ and $dt = 1$ ms. Parameters are given their corresponding values in Table 4.1, and ρ and s_0 are given as 4 cm and 1.3 cm, respectively. The resistance R is swept according to the variable load resistance values used in the experiments. Parameters p, q_1 and q_2 are used to optimize the model output such that the normalized mean squared error between the experiments and model outputs are minimized. This is formulated as an unconstrained optimization problem as follows:

$$\underset{p,q_1,q_2}{\text{minimize}} \quad \frac{||V_{ref} - \hat{V}||^2}{||V_{ref} - \frac{1}{N}\Sigma_{n=1}^{N} V_{ref}||^2}$$

Where V_{ref} is the experimental voltage recording, and $\hat{V}$ is the model voltage output given by Eq. 3.13. The first two seconds of the model output is excluded from waiting until the model converges to the steady-state solution. This optimization problem is solved by the *fminsearch* function in MATLAB.

From the obtained voltage waveforms, root-mean-square voltages V_{rms} are calculated. Then, RMS power P_{rms} values are calculated.

The forces acting on the piezoelectric patch varies according to the input actuation, which results in different strains induced in the piezoelectric material. Consequently, these parameters are fitted separately for each different configuration in the experiments. For example, different parameters are fitted for 90°–1 Hz experiments and 60°–1 Hz experiments of the piezoelectric patch MFC8528P2. Therefore, a total of 8 parameter sets are calculated that correspond to different input configurations used in the experiments.

Chapter 4

EXPERIMENTS & EVALUATION

Previous studies showed that the energy harvesting potential at the knee is higher than other joints due to higher torque at this position [21]. Therefore, we choose the human knee as the target joint to place the piezoelectric patch and evaluate energy harvesting potential during walking.

4.1 Initial Study

To study the effect of bending on the piezoelectric patch, we came up with a test setup using the Bioloid Premium kit, which is described below. The main components of this setup consisted of:

- Dynamixel AX-12A Servo motors [54]
- Bioloid Premium Kit Links [54]
- CM 530 [54]
- Foam enclosure
- Textile based enclosure

Construction: A human leg-like mechanical frame was assembled using the mechanical parts provided in the kit. This frame was covered using a foam cylinder cut in half lengthwise. Horizontal cuts were made on the foam to allow the mechanical frame to bend freely. The frame was covered entirely using a tight-fitting textile-based cover.

Actuation: The test setup is actuated using a Dynamixel AX-12A servo motor for controlled speed and angle. The motor is controlled using the dedicated CM-530 control board.

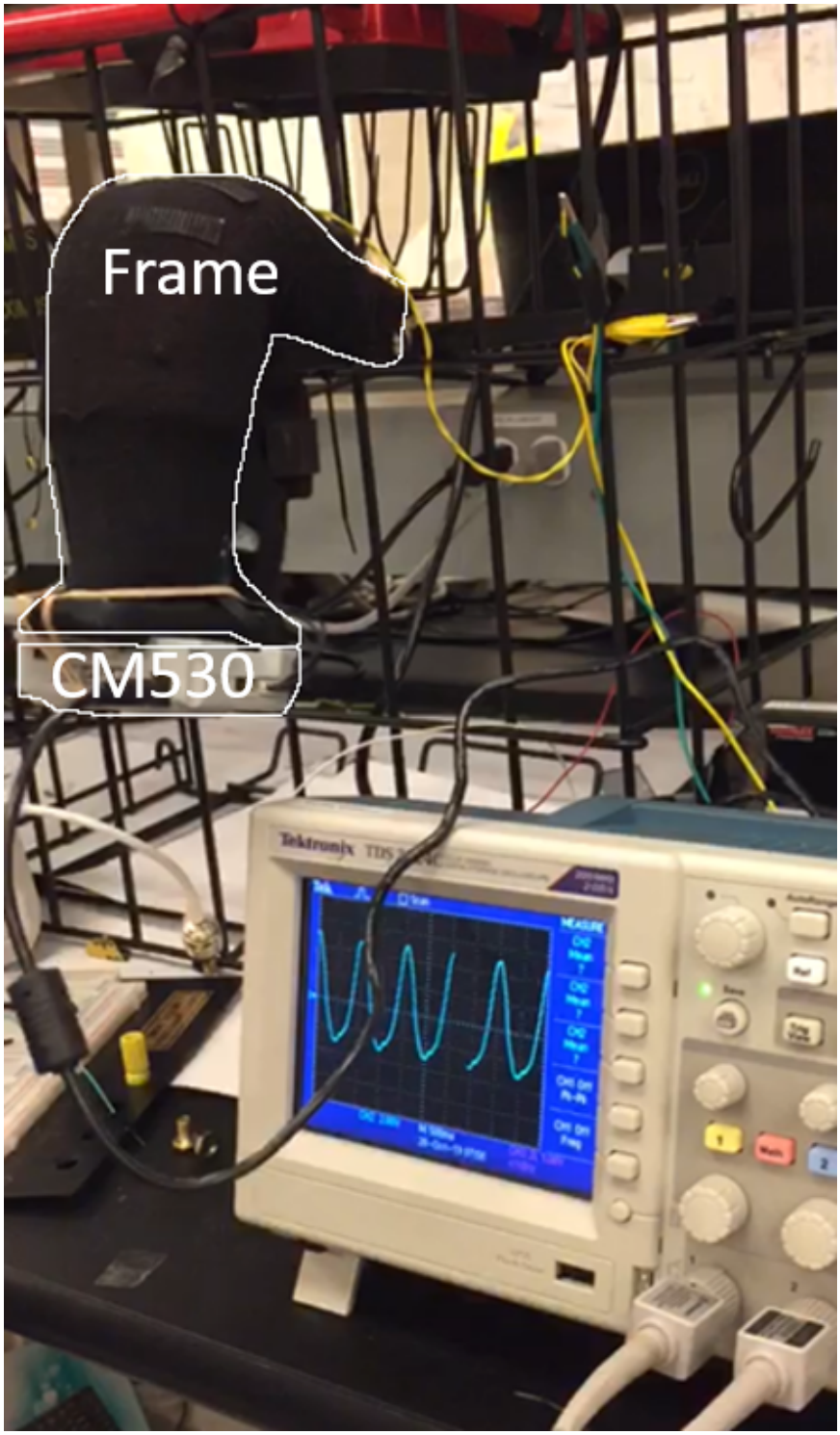

Figure 4.1: Test setup used for initial study of piezoelectric patches.

Placement: The piezoelectric patch is placed inside the test setup between the layers foam and textile-based cover, as shown in the figure 4.1. The piezoelectric element is connected to a load and an oscilloscope to study its characteristics.

An example piezoelectric output from this setup is shown in Figure 4.2

The initial study, based on this test setup, gave crucial insights into the piezoelectric patch's behavior. Some critical take-away are as follows:

- A voltage generates across the piezoelectric material's terminals only in the presence of a time-varying strain.
- When strain is first increased and then left constant, the output voltage first increases to the maximum level and decreases exponentially, with a time constant dependent on the load connected to it, similar to a capacitor discharging.

4.2 Experimental Setup Design

Design & Fabrication: Although the initial study gave crucial insights into the behavior of the piezoelectric patch, it had several pitfalls:

- The frame imparted an unknown and inconsistent bending radius onto the piezoelectric patch.
- The piezoelectric patch had unstable coupling with the frame.
- The frame induced unwanted and inconsistent strain on the piezoelectric patch.
- The frame imparted a high load on the driving motor.
- Low repeatability due to the factors discussed above.

Reproducible and controlled experiments are crucial for a systematic validation study. To this end, we design a new mechanical frame that mimics the bending of the human knee

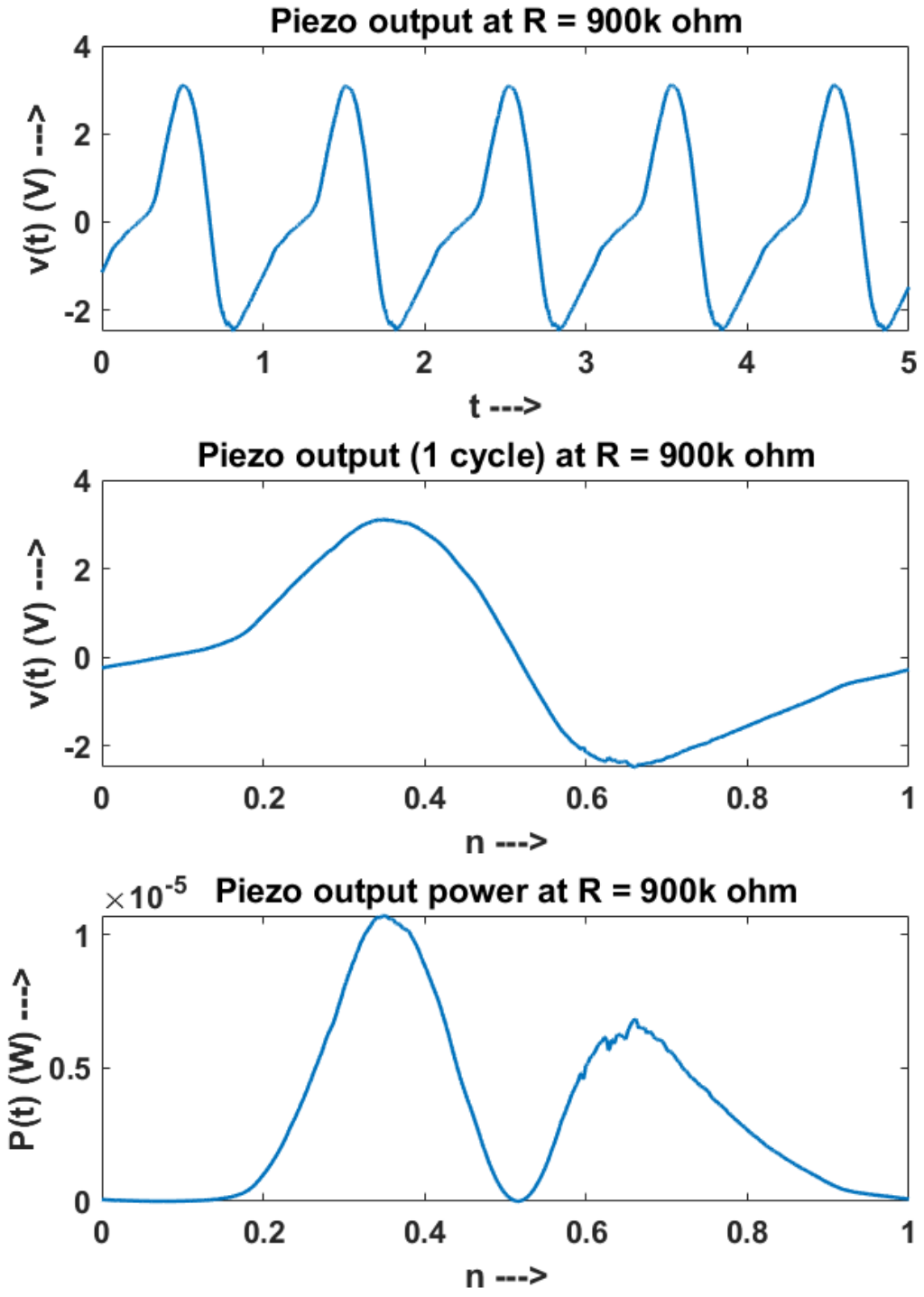

Figure 4.2: Example output from the test setup used for initial study of piezoelectric patches.

joint and, at the same time, overcomes the problems mentioned before, as shown in Figure 4.3-a).

It is composed of the upper-leg, kneecap, and lower-leg parts. The kneecap now has a known radius of curvature of 4 cm (r in Figure 3.1). Along all the three sections, a groove is present to place the piezoelectric patch for achieving near-perfect coupling to the motion. Also, screw holes are placed along the length of the frame for mounting clamps to fix the piezoelectric patch. The frame is 3D printed using acrylonitrile butadiene styrene (ABS) plastic with a 60% density for rapid prototyping. Once the new mechanical frame was assembled, the immediate problem was the smoothness in motion due to errors in 3D printing. This problem was solved by smoothening all sliding surfaces and further applying petroleum jelly based lubricant to improve smoothness.

The known problems are overcome by the new setup as follows:

Problem & Solution

- The presence of soft materials in the construction of the frame resulted in an unknown and inconsistent bending radius of the piezoelectric patch.
  - To solve this, the kneecap was fabricated with a known radius of 4cm.

- Due to the absence of a system to hold the piezoelectric patch in place, the coupling between the piezoelectric patch and the frame was unstable.
  - Groove along the whole frame to allow free movement of the piezoelectric patch and clamp at one end to hold it in place.

- The frame put the piezoelectric patch under unwanted and inconsistent strain.
  - External factors like a textile-based cover, which interfered with the piezoelectric patch, were replaced by a smooth cover for the patch to slide inside.

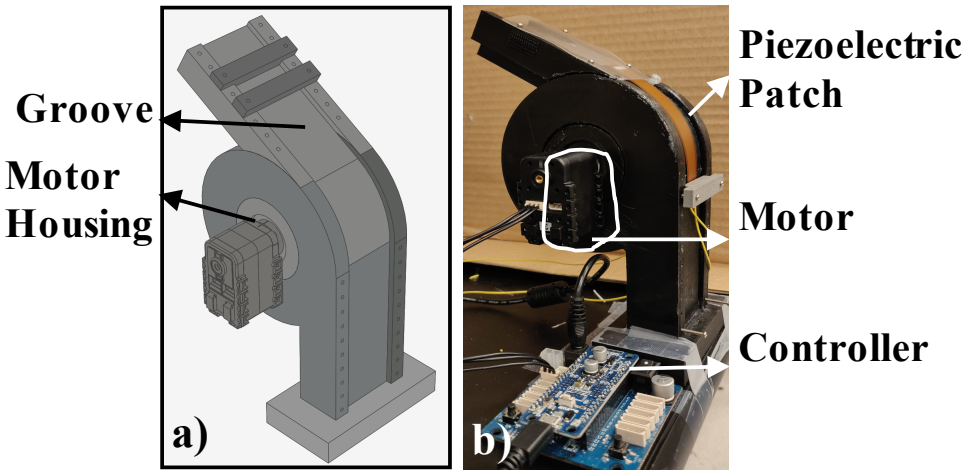

Figure 4.3: Mechanical human knee joint a) design in SolidWorks, b) 3D printed

- Due to the restrictive nature of foam, the driving motor experienced high load

  - Free movement of the knee joint and lightweight construction ensured low motor load.

Actuation: A Dynamixel AX-12A servo motor is used to actuate the frame for controlled speed and angle. Potential timing errors that may arise due to the use of a non-real-time OS, such as inconsistencies in the input waveform, are avoided by controlling the motor through the dedicated OpenCMv9.04 control board.

Placement: The piezoelectric patch is clamped to the lower-leg from one end. Then the other end of the piezoelectric patch is covered to contain it in the upper leg, as shown in Figure 4.3-b). The distance from the clamped end to the curved surface is measured to be 1.3 cm (s_0 in Figure 3.1). The other end of the piezoelectric patch is left free to avoid any extra strain and allow free motion. Besides, extra care was taken to avoid pressure onto the piezoelectric patch along the frame to avoid additional forces due to friction.

We used a digital oscilloscope for real-time visualization of the waveform produced by bending the piezoelectric patch and a resistance box to capture the resistive load effect on the patch. The NI DAQ system was used to acquire accurate data.

4.2.1 Test and Debug of the Experimental Setup

Before proceeding with experiments using piezoelectric patches, the goodness of the experimental setup had to be established. It was evaluated if the test setup indeed overcame the issues with the initial setup. The test parameters are as follows:

- Smooth movement of the 3D printed knee.

  Once the new mechanical frame was assembled, the immediate problem was the smoothness in motion due to 3D printing errors. This problem was solved by smoothening all sliding surfaces using a filer and sandpaper and further applying petroleum jelly based lubricant to improve smoothness.

- Verify if the test setup can move at the required speed.

  For our experiments, we needed the test setup to actuate at least 90°, 1Hz, without any jitters. For this, both actuation amplitude and frequency were swept. No noticeable jitter was present in our points of interest. However, There were jitters when the amplitude was set to below 30 degrees or below 0.25 Hz.

- Use angular displacement sensor to verify the accuracy of the movement.

  An Angular Displacement Sensor (ADS) manufactured by Bendlabs [10] was placed on the mechanical frame to verify the movement's accuracy. Data obtained from this sensor is shown in AppendixA. The setup proved to be accurate up to $\pm 2°$.

- Determine the maximum capability of the setup.

  With the ADS mounted on the frame; it was actuated at 90°, 1Hz. Then the frequency of operation was increased by in steps of 0.1 Hz while keeping the amplitude constant. I was repeated until the frame was unable to bend the whole of 90° at the required frequency. The frame could achieve up to 90°, 1.5Hz operation.

- Check if repeatable measurements were obtained from the piezoelectric patch mounted on the knee.

  A piezoelectric patch was mounted on the frame as described in section 4.3. It was actuated at 90°, 1Hz with a load of 1MΩ. This process was repeated, and the effect was observed. No significant change in output waveform was observed, thereby establishing the repeatability of experiments performed using the new frame.

4.3 Experimental Methods and Procedure

Piezoelectric Materials: We validate the proposed models using two different MFC elements, the MFC8514P2 and the MFC8528P2 [56]. The parameters of these devices are summarized in Table 4.1.

Figure 4.4: Macro Fiber Composite (MFC) Patchs, MFC8528P2 and MFC8514

Excitation Input: We use four different sinusoidal excitations with the following bending angle and frequency pairs: (60°; 0.5 Hz), (60°; 1 Hz), (90°; 0.5 Hz), and (90°; 1 Hz). For example, the pair (60°; 0.5 Hz) means that the knee bends by 60° degrees starting from a neutral position, and the movement is repeated with a frequency of 0.5 Hz. For each input, the rotation angle is recorded with a Bendlabs angle measurement sensor [10] placed on the frame to verify that the actuation matches the input excitation and uses it as an input to the developed energy harvesting model.

Load: We sweep the load connected to the MFC elements from 100 kΩ to 10MΩ for each input excitation. The load is swept 100 kΩ increments between 100 kΩ and 1 MΩ, and 200 kΩ increments between 1 MΩ and 10 mΩ. For each load, we record the generated voltage for ten seconds with NI DAQ.

Experiment Duration: All experiments have been repeated twice to eliminate any human-related errors during data recording. Therefore, a total of 16 experiments were performed for the analysis part in this work (4 angle-frequency pairs $\times$ 2 piezoelectric elements $\times$ 2 sets of measurements) are carried out *for each load*. Each experiment takes approximately four hours with post-processing, which involved phase aligning and indexing, followed by grouping and averaging. Finally, the root mean square (RMS) voltage values and RMS power calculation. Hence, the measurements used in this study took about 64 staff-hours. However, more experiments covering PVDF and MFC models with 45° excitation were also performed, which have not been analyzed in this work, but included as a contribution to our data set.

4.4 Validation Under Controlled Experiments

The proposed model predicts the generated voltage as a function of time. Then, the generated power is computed using the output voltage. Therefore, we summarize the accuracy

Table 4.1: Geometrical and physical parameters of the MFC elements used in experimental validation.

	MFC8514P2	MFC8514P2
W (mm)	28	14
C (nF)	264±20%	138±20%
L (mm)	85	85
h_p (μm)	180	180
Y_p (GPa)	30.336	30.336
h_s (μm)	120	120
Y_s (GPa)	2.8	2.8
d_{31} (pC/N)	-170	-170
r (cm)	4	4
s_0 (cm)	1.3	1.3

in generating the output voltage and then present the accuracy in modeling the generated power in detail.

4.4.1 Output Voltage Comparison

As a representative example, Fig. 4.5 shows the experimental voltage recording and the corresponding model output obtained with MFC8528P2 for 90° bending angle, 1 Hz excitation frequency, and 0.4 MΩ loads. The model output closely follows the experimental voltage signal. Furthermore, it achieves 2.71% mean absolute percentage error (MAPE). In general, the MAPE of the proposed model ranges from 0.78% to 3.55% for all experiments with different bending angles and frequency pairs.

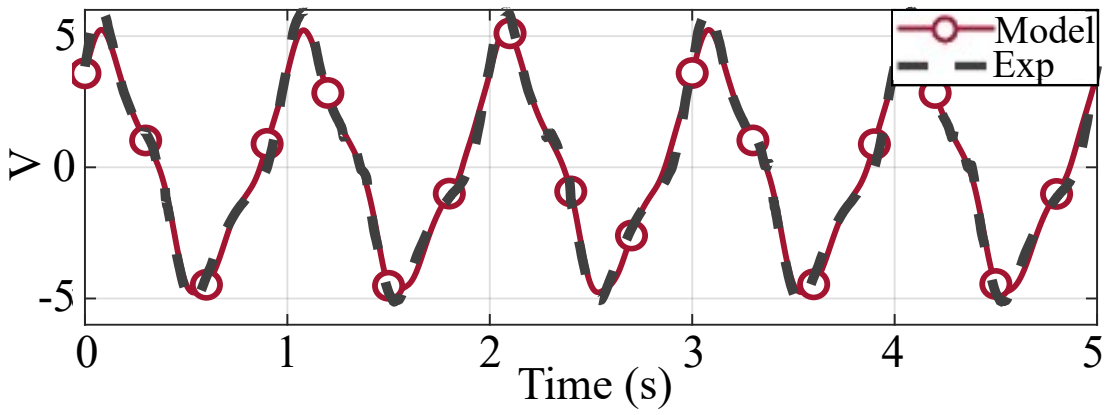

Figure 4.5: Voltage output of MFC8528P2. Input: 90° bending angle, 1 Hz excitation frequency. Load: R_{Load} = 0.4 MΩ

4.4.2 Output Power Comparison

Next, we analyze the generated power P_{RMS} in detail as a function of all input parameters and the load. Fig 4.6-a and Fig 4.6-b plot the measured P_{RMS} and model results obtained from MFC85**28**P2 (larger). In Fig 4.6-a, the MAPE of the proposed model is 5.36% and 5.34% for (90°; 1 Hz) and (60°; 1 Hz) input excitations, respectively. In Fig 4.6-b, the MAPE of the proposed model is 4.09% and 4.04% for (90°; 0.5 Hz) and (60°; 0.5 Hz) input excitations, respectively. The highest experimental power is approximately 26 μW for 90°–1 Hz excitation of MFC8528P2. The model prediction for the same point is approximately 24.5 μW. Similarly, fig. 4.7 shows the P_{RMS} values at 0.5 Hz excitation. In this case, the highest experimental power is approximately 12.4 μW for 90°–0.5 Hz excitation of MFC8528P2. The model prediction for the same point is approximately 12 μW. When all curves are considered, the average mean-absolute-percentage-error is 4.8%. Similarly, Fig 4.7-a and Fig 4.7-b show the same results for MFC85**14**P2 (smaller). Fig 4.7-a shows that the MAPE of the proposed model is 3.55% and 1.54% for (90°; 1 Hz) and (60°; 1 Hz)

input excitations, respectively. Fig 4.7-b shows that the MAPE of the proposed model is 6.94% and 3.79% for (90°; 0.5 Hz) and (60°; 0.5 Hz) input excitations, respectively.

There are three key observations from these results:

The bending angle does not shift the maximum power point (MPP). It only affects the magnitude of the generated power. For example, Fig 4.6-a) shows that the MPP is R_{Load}=0.4 MΩ element under 1 Hz excitation for both 90° and 60° bending angles. Similarly, the MPP does not change for the smaller piezoelectric elements and 0.5 Hz frequency, as shown in Fig 4.6 and Fig. 4.7. In all cases, the MPP predicted by the proposed model matches the measurements.

The excitation frequency affects both the magnitude and the load value for the MPP. For instance, the MPP shifts from 0.4 MΩ to 0.8 MΩ when the excitation frequency decreases from 1 Hz to 0.5 Hz (see Fig 4.6-a) and Fig. 4.7-a)). This observation is in agreement with the first-order approximation of a piezoelectric patch as a capacitance. In an RC circuit, maximum power transfer occurs at R=$\frac{1}{2\pi fC}$. Therefore, R is inversely proportional to both

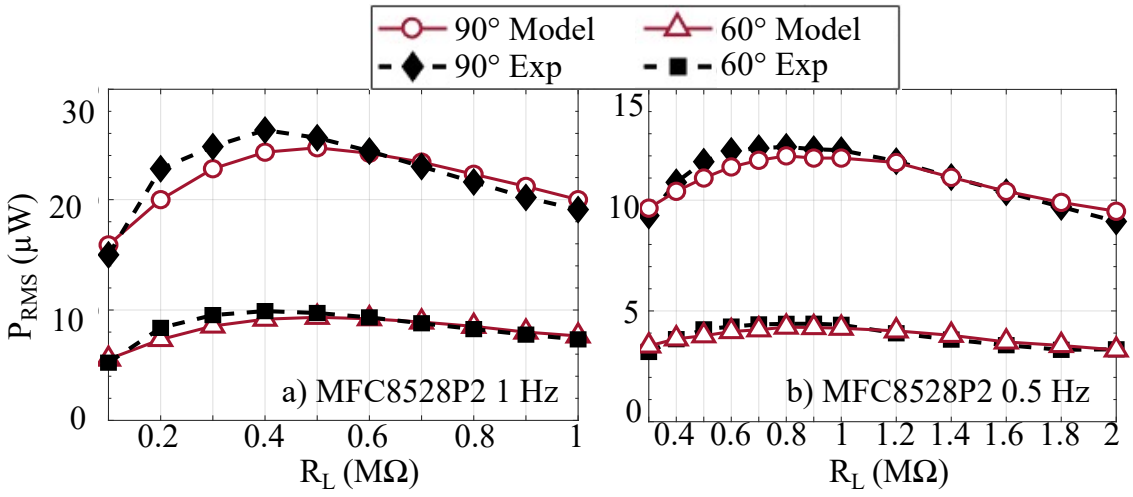

Figure 4.6: P_{RMS} for MFC8528P2 a) 1 Hz b) 0.5 Hz

the excitation frequency and the capacitance of the piezoelectric element. We also note that the generated power decreases with the excitation frequency as expected.

The size of the piezoelectric patch also affects both the magnitude and the load value for the MPP. Smaller size yields less power due to smaller piezoelectric material volume, hence, smaller dielectric displacement. Due to the smaller patch's lower capacitance, the maximum power point also shifts to higher load values. For example, when Fig 4.6-a) and b) are considered, going from the larger MFC8528P2 to the smaller MFC8514P2 shifts the MPP from 26 μW at R_{Load}=0.4 MΩ to 14.7 μW at R_{Load}=0.8 MΩ. It is expected since the maximum power transfer occurs at R=$\frac{1}{\omega C}$, as noted above.

4.5 Applications to Real Life Scenarios

This section illustrates the application of the proposed methodology to real-life scenarios. To this end, we recorded the user's knee angle during walking using a Bendlabs angular displacement sensor sensor [10]. As an example, Fig. 4.8-a) shows the recorded knee angle from the right knee of the subject. It is observed that the bending angle is close

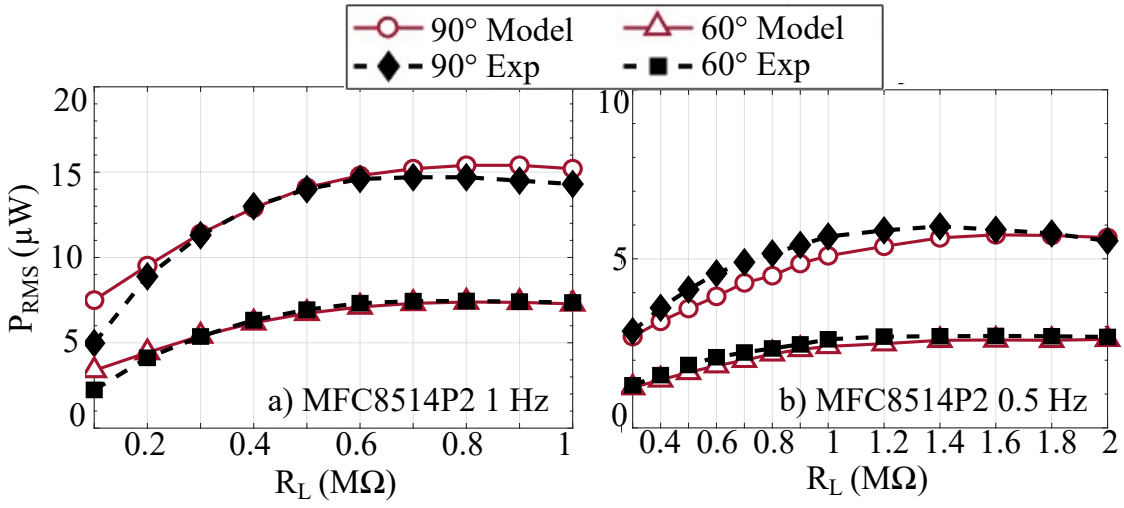

Figure 4.7: P_{RMS} for MFC8514P2 a) 1 Hz b) 0.5 Hz

to 60°, and frequency is slightly smaller than 1 Hz. Hence, we can predict the harvested energy using the model parameters found in the previous section.

We consider MFC8528P2 as the piezoelectric element and the maximum power point, i.e., R_{Load}=0.4 MΩ, to analyze the energy harvesting potential. First, the measured knee angle waveform is fed as input to the proposed model to find the output voltage. The generated voltage leads to 6.5 μW RMS power with a 0.4 MΩ load. Considering both knees, we argue that 13 μW power can be generated by this user while walking.

Next, we investigate the use of the generated power for wearable applications. The run-time use of the model is illustrated as an MPP tracking algorithm for human motion energy harvesting applications. Different parameter sets that correspond to different amplitude and frequency pairs are stored on the device. During operation, a run-time algorithm inspects the generated voltage and identifies the frequency of the motion. The parameter set for the obtained amplitude and frequency pair is used to estimate the magnitude of the excitation angle. It proceeds to calculate the power curve and determine the MPP. Finally, the application sets its input impedance such that it corresponds to the calculated MPP.

Once we know the amount of energy harvested, we can evaluate it's goodness for a given application in terms of duty ratio. Let the duty ratio be the percentage of time a wearable device can be powered by the harvested energy. Fig. 4.8-b) shows the obtained duty ratio for the hypothetical design spanning the [1 μW, 1 mW] interval. If the device's power consumption is less than 13 μ W, then the piezoelectric element can power it perpetually, while devices with larger power consumption must turn off periodically. Also, we used examples of low-power wearable application studies from the literature [68, 66, 33]. For example, for an application that consumes 100 μW, the duty ratio is 13%. For this approach, the generated energy is stored for 10 seconds and uses the stored energy to run the application for 1.3 seconds. We argue that 1.3 seconds is usually sufficient for wearable applications to sample and process data due to the slow dynamics of the human body. Thus,

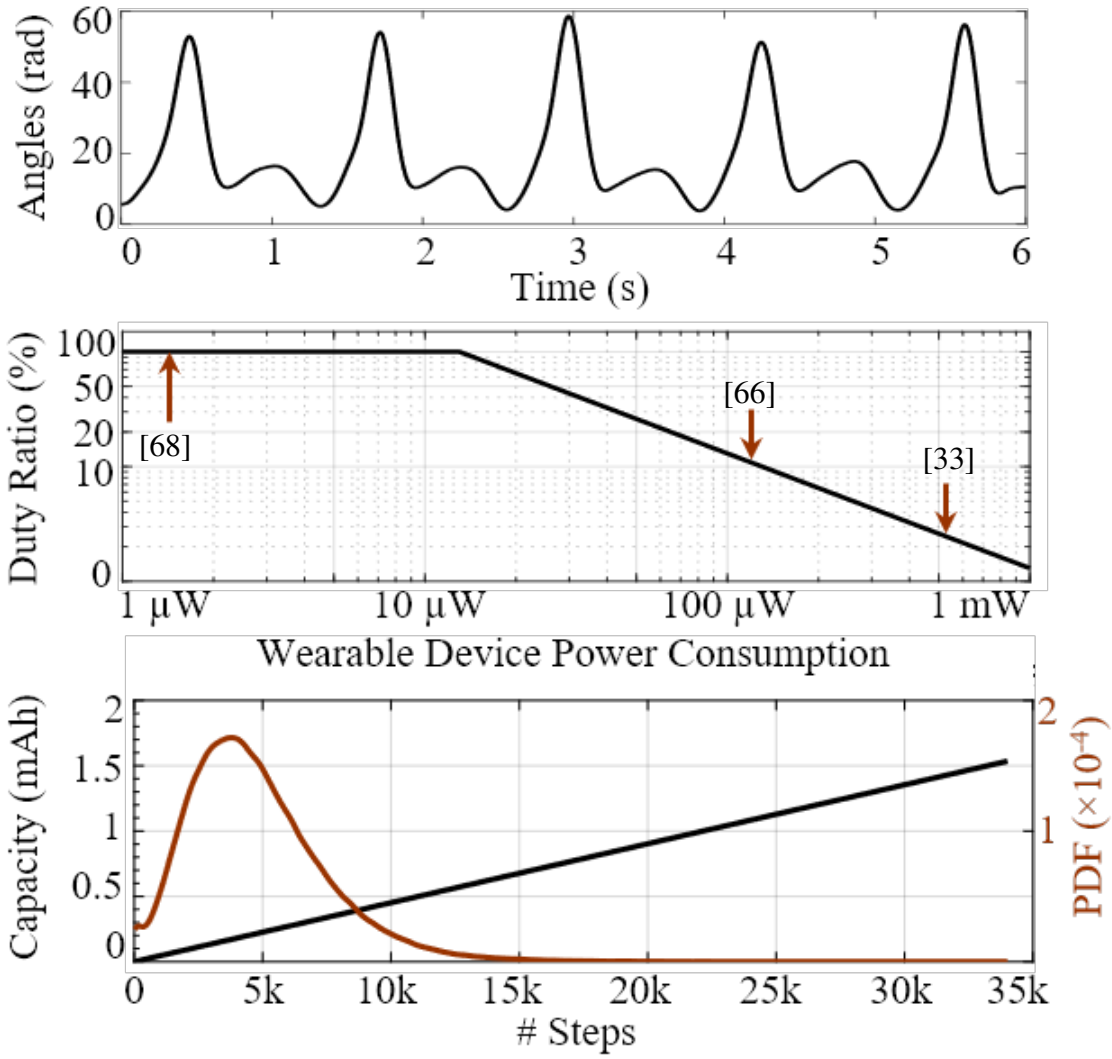

Figure 4.8: a) Knee angle during walking b) Duty cycle c) Battery equivalent [68]

for every 10 seconds on energy generation, we power our device for 1.3s. An example is a device presented in [66] that has 137 μW power consumption; hence it can be powered with a 9.4% duty cycle.

Finally, the cumulative energy harvested for this person as a function of the number of steps is analyzed. The probability distribution function (PDF) depicted in Fig. 4.8-c) (right axis) shows that an average person takes less than 10000 steps in a day [3]. Assuming each

step takes 1.2 seconds, 7.8 μJ of energy would be harvested per step. Therefore, a person who takes 7500 steps a day, $30 \times 7500 \times 7.8$=1.75 J would be harvested in a month. This corresponds to a battery with 0.40 mAh charge capacity rated at 1.2V. Fig. 4.8-c) illustrates the predicted charge capacity for a different number of steps daily.

4.6 Energy Harvested in a System

This section demonstrates the energy harvesting from the MFC8528P2 piezoelectric patch using the EH300A energy harvesting module [1] (Figure 4.9). The EH300A module takes input from energy harvesting sources, such as piezoelectric patches, rectifies the input, and stores the energy for later use. The piezoelectric patch was mounted on the frame. It was connected to the input terminal of the EH300A module, and the frame was actuated at 90°, 1Hz.

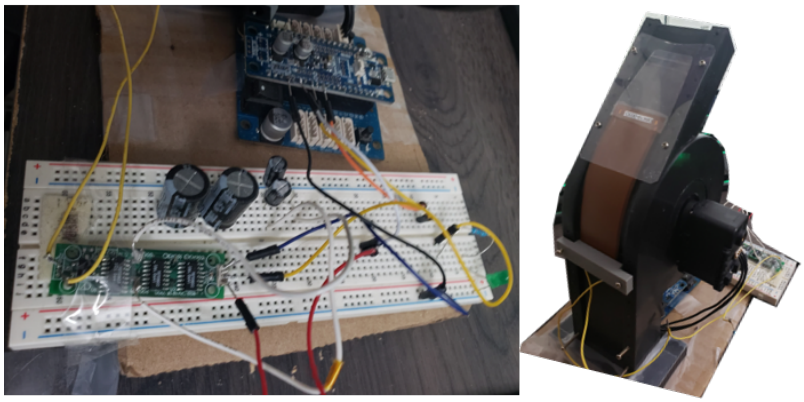

Figure 4.9: Experimental setup with EH300A connected with 100 μf storage capacitor

The EH300A module has a 6600 μf storage capacitor. However, the EH300A energy harvesting module does not have a matching input impedance with the piezoelectric patch. As this study clearly shows that impedance matching is necessary for maximum energy harvesting, the EH300A module is unable to harvest all the energy produced by the piezoelectric patch, thereby charging the storage capacitor slowly. The amount of energy required to

charge the capacitor is reduced for quick demonstration purposes by modifying the module by replacing the original 6600 μf storage capacitor with 100 μf storage capacitor. This approach reduced the amount of energy required to charge the capacitor. The voltage on the storage capacitor was monitored by the Vp output pin of the module using the on-board ADC of the OpenCM 9.04 module. The corresponding voltage curve is shown in Fig 4.10.

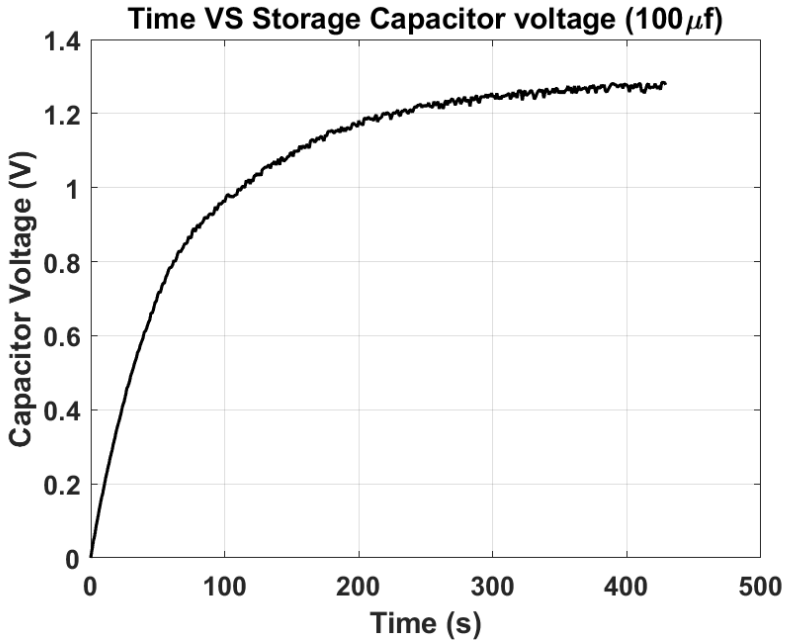

Figure 4.10: Voltage curve of the 100 μf storage capacitor, when MFC8528P2 is actuated at 90°, 1 Hz

The capacitor takes 420s to charge the capacitor from 0V to 1.27V, by harvesting 80 μJ energy, i.e., the power generated is close to 0.2 μW, which is very less than the earlier experimental result of 26 μW even after considering an efficiency factor of the harvesting circuitry. This effect is possibly due to the impedance mismatch between the piezoelectric patch and the input of the EH300A module. Some approaches to fix this are a look-up table based MPPT tracking algorithm and an adaptive impedance circuit.

Chapter 5

CONCLUSION AND FUTURE WORK

The increasing popularity of wearable technology and low power design has inspired research on energy harvesting directly from human motion. Among many different methodologies for energy harvesting, piezoelectric energy harvesting provides an attractive solution to wearable devices. Consequently, various researchers have shown different approaches to piezoelectric energy harvesting from human motion. However, these approaches proved to be usually too bulky and hence impractical for the daily user. This work considered flexible piezoelectric patches coupled directly on a human joint, which involves large movements to evaluate the practicability of piezoelectric energy harvesting from human motion. We present a study that involves experimental evaluations used to verify a mathematical model for flexible piezoelectric patches placed on joints. Initially, the properties of piezoelectric patches are studied using an easy to implement experimental setup. Then, we analyzed the requirements for performing reliable experiments and design an experimental setup using CAD tools. Then the parts of a novel experimental setup are designed in CAD and fabricated with a 3D printer and assemble them. The 3D printed setup is validated using the ADS sensor to ensure minimal errors while performing experiments. We performed experiments using the chosen MFC patches and then proved the validity of the mathematical model using the experimental data by curve fitting. In this work, we used two excitation frequencies (0.5 Hz and 1 Hz) and two bending angles (60° and 90°) for validation of the mathematical model.

Once the model's validity was established, it was used to project the energy harvesting potential from walking. According to our results, 13 μW can be harvested from the knees during walking. Furthermore, we estimate that the monthly charge capacity generated by

a person that regularly walks 7500 steps/day is equivalent to that of a 0.40 mAh 1.2V battery. To prove the feasibility of human motion energy harvesting, We used a commercially available energy harvesting circuit and charged a storage capacitor using the MFC patch. It showed that an adaptive impedance matching system is necessary for optimal energy harvesting from piezoelectric materials. These observations motivated us to plan the next steps beyond this work.

Future work:

- As Human motion involves various frequencies and knee angles, the mathematical model must be verified for the full range of relevant angles and frequencies. We, therefore, intend to extend the experimental dataset to a finer granularity.

- We will also capture different motion sequences. For example, elbow patterns, walking and running. Repeatable experiments will be performed using these captured motion sequences through our experimental setup. Performing the new experiments will require an experimental setup that can actuate faster than our current version. So, an improved experimental setup to accommodate the new needs will be designed.

- We also plan to apply the proposed technique to other piezoelectric materials.

- Furthermore, a commercially available adaptive input impedance system will be used to harvest energy. Also, an energy harvesting system with adaptive input impedance will be designed.

- Finally, the harvester will be mounted on various joints of a human subject, and the harvested energy from various activities will be evaluated.

REFERENCES

[1] Advanced Linear Devices, Inc. EH300/EH301 EH Modules. [Online] https://www.aldinc.com/pdf/EnergyHarvestingModules.pdf/, accessed May 2020.

[2] P. Ahmmed, J. Dieffenderfer, J. M. Valero-Sarmiento, V. R. Pamula, N. Van Helleputte, C. Van Hoof, M. Verhelst, and A. Bozkurt. A wearable wrist-band with compressive sensing based ultra-low power photoplethysmography readout circuit. In *2019 IEEE 16th International Conference on Wearable and Implantable Body Sensor Networks (BSN)*, pages 1–4, May 2019.

[3] T. Althoff, J. L. Hicks, A. C. King, S. L. Delp, J. Leskovec, et al. Large-scale physical activity data reveal worldwide activity inequality. *Nature*, 547(7663):336–339, 2017.

[4] Y. Bai, P. Tofel, Z. Hadas, J. Smilek, P. Losak, P. Skarvada, and R. Macku. Investigation of a cantilever structured piezoelectric energy harvester used for wearable devices with random vibration input. *Mechanical Systems and Signal Processing*, 106:303–318, 2018.

[5] S. Balguvhar and S. Bhalla. Green energy harvesting using piezoelectric materials from bridge vibrations. In *2018 2nd International Conference on Green Energy and Applications (ICGEA)*, pages 134–137, 2018.

[6] A. J. Bandodkar, P. Gutruf, J. Choi, K. Lee, Y. Sekine, J. T. Reeder, W. J. Jeang, A. J. Aranyosi, S. P. Lee, J. B. Model, et al. Battery-free, skin-interfaced microfluidic/electronic systems for simultaneous electrochemical, colorimetric, and volumetric analysis of sweat. *Science advances*, 5(1):eaav3294, 2019.

[7] M. Bariya, H. Y. Y. Nyein, and A. Javey. Wearable sweat sensors. *Nature Electronics*, 1(3):160–171, 2018.

[8] G. Bassani, A. Filippeschi, and E. Ruffaldi. Human motion energy harvesting using a piezoelectric mfc patch. 08 2015.

[9] G. Bassani, A. Filippeschi, and E. Ruffaldi. Nonresonant kinetic energy harvesting using macrofiber composite patch. *IEEE Sensors Journal*, 18(5):2068–2076, 2018.

[10] Bend Labs. Flexible Single Axis Bidirectional Sensor, 2019. [Online] https://www.bendlabs.com/products/1-axis-evaluation-kit/, accessed 26 Nov. 2019.

[11] G. Bhat, K. Bagewadi, H. G. Lee, and U. Y. Ogras. Reap: Runtime energy-accuracy optimization for energy harvesting iot devices. In *2019 56th ACM/IEEE Design Automation Conference (DAC)*, pages 1–6, 2019.

[12] G. Bhat, R. Deb, V. V. Chaurasia, H. Shill, and U. Y. Ogras. Online human activity recognition using low-power wearable devices. In *2018 IEEE/ACM International Conference on Computer-Aided Design (ICCAD)*, pages 1–8, 2018.

[13] G. Bhat, R. Deb, and U. Y. Ogras. Openhealth: Open-source platform for wearable health monitoring. *IEEE Design & Test*, 36(5):27–34, 2019.

[14] G. Bhat, U. Gupta, N. Tran, J. Park, S. Ozev, and U. Y. Ogras. Multi-objective design optimization for flexible hybrid electronics. In *Proceedings of the 35th International Conference on Computer-Aided Design*, pages 1–8, 2016.

[15] G. Bhat, J. Park, and U. Y. Ogras. Near-optimal energy allocation for self-powered wearable systems. In *2017 IEEE/ACM International Conference on Computer-Aided Design (ICCAD)*, pages 368–375, 2017.

[16] G. Bhat, Y. Tuncel, S. An, H. G. Lee, and U. Y. Ogras. An ultra-low energy human activity recognition accelerator for wearable health applications. *ACM Transactions on Embedded Computing Systems (TECS)*, 18(5s):1–22, 2019.

[17] A. Cammarano, D. Spenza, and C. Petrioli. Energy-harvesting wsns for structural health monitoring of underground train tunnels. In *2013 IEEE Conference on Computer Communications Workshops (INFOCOM WKSHPS)*, pages 75–76, 2013.

[18] Y. Cha. Energy harvesting using flexible piezoelectric materials from human walking motion: Theoretical analysis. *Journal of Intelligent Material Systems and Structures*, 28(20):3006–3015, 2017.

[19] Y. Cha. Energy harvesting using flexible piezoelectric materials from human walking motion: Theoretical analysis. *Journal of Intelligent Material Systems and Structures*, 28(20):3006–3015, 2017.

[20] C. Chen, L. Y. Chau, and W.-H. Liao. A knee-mounted biomechanical energy harvester with enhanced efficiency and safety. *Smart Materials and Structures*, 26(6):065027, may 2017.

[21] Y.-M. Choi, M. G. Lee, and Y. Jeon. Wearable biomechanical energy harvesting technologies. *Energies*, 10(10):1483, 2017.

[22] T. Daue and J. Kunzmann. Energy harvesting systems using piezo-electric mfcs. 1:1–1, 02 2008.

[23] N. G. Elvin and A. A. Elvin. Large deflection effects in flexible energy harvesters. *Journal of Intelligent Material Systems and Structures*, 23(13):1475–1484, 2012.

[24] A. Erturk and D. J. Inman. A Distributed Parameter Electromechanical Model for Cantilevered Piezoelectric Energy Harvesters. *Journal of Vibration and Acoustics*, 130(4), 2008.

[25] M. Geisler, S. Boisseau, P. Gasnier, J. Willemin, C. Gobbo, G. Despesse, I. Ait-Ali, and S. Perraud. Looped energy harvester for human motion. *Smart Materials and Structures*, 26(10):105035, sep 2017.

[26] M. Geisler, S. Boisseau, M. Perez, P. Gasnier, J. Willemin, I. Ait-Ali, and S. Perraud. Human-motion energy harvester for autonomous body area sensors. *Smart Materials and Structures*, 26(3):035028, feb 2017.

[27] U. Gupta, J. Park, H. Joshi, and U. Y. Ogras. Flexibility-aware system-on-polymer (sop): Concept to prototype. *IEEE Transactions on Multi-Scale Computing Systems*, 3(1):36–49, 2016.

[28] R. Hamid and M. R. Yuce. A wearable energy harvester unit using piezoelectric–electromagnetic hybrid technique. *Sensors and Actuators A: Physical*, 257:198–207, 2017.

[29] I. Izadgoshasb, Y. Y. Lim, N. Lake, L. Tang, R. V. Padilla, and T. Kashiwao. Optimizing orientation of piezoelectric cantilever beam for harvesting energy from human walking. *Energy Conversion and Management*, 161:66 – 73, 2018.

[30] H. Jeong et al. Modular and reconfigurable wireless e-tattoos for personalized sensing. *Adv. Mater. Technol.*, 4(8):1900117, 2019.

[31] S. Ju, S. H. Chae, Y. Choi, S. Jun, S. M. Park, S. Lee, H. W. Lee, and C. . Ji. Harvesting energy from low frequency vibration using msma/mfc laminate composite. In *2013 Transducers Eurosensors XXVII: The 17th International Conference on Solid-State Sensors, Actuators and Microsystems (TRANSDUCERS EUROSENSORS XXVII)*, pages 1348–1351, June 2013.

[32] S. Kang, J. Lee, K. Bong, C. Kim, and H. Yoo. A 0.53mw ultra-low-power 3d face frontalization processor for face recognition with human-level accuracy in wearable devices. In *2017 IEEE International Symposium on Circuits and Systems (ISCAS)*, pages 1–4, May 2017.

[33] S. Kang, J. Lee, K. Bong, C. Kim, and H.-J. Yoo. A 0.53 mw ultra-low-power 3d face frontalization processor for face recognition with human-level accuracy in wearable devices. In *IEEE ISCAS*, pages 1–4, 2017.

[34] Y. Khan et al. Flexible Hybrid Electronics: Direct Interfacing of Soft and Hard Electronics for Wearable Health Monitoring. *Advanced Functional Materials*, 26(47):8764–8775, 2016.

[35] Y. Kuang, Z. Yang, and M. Zhu. Design and characterisation of a piezoelectric knee-joint energy harvester with frequency up-conversion through magnetic plucking. *Smart Materials and Structures*, 25(8):085029, 2016.

[36] L. K. Lam and A. J. Szypula. Wearable emotion sensor on flexible substrate for mobile health applications. In *2018 IEEE Sensors Applications Symposium (SAS)*, pages 1–5, March 2018.

[37] V. Leonov. Thermoelectric energy harvesting of human body heat for wearable sensors. *IEEE Sensors Journal*, 13(6):2284–2291, 2013.

[38] H. Liu, C. J. Tay, C. Quan, T. Kobayashi, and C. Lee. Piezoelectric mems energy harvester for low-frequency vibrations with wideband operation range and steadily increased output power. *Journal of Microelectromechanical Systems*, 20(5):1131–1142, Oct 2011.

[39] H. Liu, J. Zhong, C. Lee, S.-W. Lee, and L. Lin. A comprehensive review on piezoelectric energy harvesting technology: Materials, mechanisms, and applications. *Applied Physics Reviews*, 5(4):041306, 2018.

[40] W. Liu, Z. Wang, S. Qu, and R. Luo. Vibration energy harvesting and management for wireless sensor networks in bridge structural monitoring. In *2015 IEEE SENSORS*, pages 1–4, 2015.

[41] P. A. Lopes, D. Vaz Gomes, D. Green Marques, P. Faia, J. Góis, T. F. Patrício, J. Coelho, A. Serra, A. T. de Almeida, C. Majidi, et al. Soft bioelectronic stickers: Selection and evaluation of skin-interfacing electrodes. *Advanced healthcare materials*, 8(15):1900234, 2019.

[42] P. Nintanavongsa, U. Muncuk, D. R. Lewis, and K. R. Chowdhury. Design optimization and implementation for rf energy harvesting circuits. *IEEE Journal on Emerging and Selected Topics in Circuits and Systems*, 2(1):24–33, 2012.

[43] A. Nk, G. Bhat, J. Park, H. G. Lee, and U. Y. Ogras. Sensor-classifier co-optimization for wearable human activity recognition applications. In *2019 IEEE International Conference on Embedded Software and Systems (ICESS)*, pages 1–4, 2019.

[44] J. A. Paradiso and T. Starner. Energy scavenging for mobile and wireless electronics. *IEEE Pervasive computing*, (1):18–27, 2005.

[45] J. Park, G. Bhat, C. S. Geyik, U. Y. Ogras, and H. G. Lee. Energy per operation optimization for energy-harvesting wearable iot devices. *Sensors*, 20(3):764, 2020.

[46] J. Park, H. Joshi, H. G. Lee, S. Kiaei, and U. Y. Ogras. Flexible pv-cell modeling for energy harvesting in wearable iot applications. *ACM Transactions on Embedded Computing Systems (TECS)*, 16(5s):1–20, 2017.

[47] P. Pillatsch, E. M. Yeatman, and A. S. Holmes. A piezoelectric frequency up-converting energy harvester with rotating proof mass for human body applications. *Sensors and Actuators A: Physical*, 206:178–185, 2014.

[48] A. Proto, M. Penhaker, D. Bibbo, D. Vala, S. Conforto, and M. Schmid. Measurements of generated energy/electrical quantities from locomotion activities using piezoelectric wearable sensors for body motion energy harvesting. *Sensors*, 16(4):524, 2016.

[49] Y. Pu, G. Samson, C. Shi, D. Park, K. Easton, R. Beraha, J. Hadi, M. Lin, E. Arvelo, J. Fatehi, J. Kumar, M. Derkalousdian, P. Aghera, A. Newham, H. Sheraji, K. Chatha, R. McLaren, V. Ganesan, S. Namasivayam, D. Butterfield, R. Shenoy, and R. Attar. Blackghost: An ultra-low-power all-in-one 28nm cmos soc for internet-of-things. In *2017 IEEE Symposium in Low-Power and High-Speed Chips (COOL CHIPS)*, pages 1–3, April 2017.

[50] F. Qian, T.-B. Xu, and L. Zuo. Design, optimization, modeling and testing of a piezoelectric footwear energy harvester. *Energy Conversion and Management*, 171:1352 – 1364, 2018.

[51] F. Qian, T.-B. Xu, and L. Zuo. Piezoelectric energy harvesting from human walking using a two-stage amplification mechanism. *Energy*, 189:116140, 2019.

[52] M. Rahimi, H. Shah, G. S. Sukhatme, J. Heideman, and D. Estrin. Studying the feasibility of energy harvesting in a mobile sensor network. In *IEEE International Conference on Robotics and Automation*, volume 1, pages 19–24, 2003.

[53] R. Ramezanpour, H. Nahvi, and S. Ziaei-Rad. Electromechanical behavior of a pendulum-based piezoelectric frequency up-converting energy harvester. *Journal of Sound and Vibration*, 370:280 – 305, 2016.

[54] Robotis Inc. Bioloid Series. [Online] `http://www.robotis.us/bioloid-1/`, accessed May 2020.

[55] S. Roundy and S. Trolier-McKinstry. Materials and approaches for on-body energy harvesting. *MRS Bulletin*, 43(3):206–213, 2018.

[56] Smart-Material. MFC P2 and P3 types. [Online] `https://www.smart-material.com/MFC-product-P2.html`, accessed May 2020.

[57] S. Sudevalayam and P. Kulkarni. Energy harvesting sensor nodes: Survey and implications. *IEEE Communications Surveys & Tutorials*, 13(3):443–461, 2010.

[58] Y. Tuncel, S. Bandyopadhyay, S. Kulshrestha, A. Mendez, and Y. Umit. Towards wearable piezoelectric energy harvesting:modeling and experimental validation. In *Proc. of International Symposium on Low Power Electronics and Design (ISLPED)*, pages Accepted, in print, 2020.

[59] A. C. Turkmen and C. Celik. Energy harvesting with the piezoelectric material integrated shoe. *Energy*, 150:556 – 564, 2018.

[60] M. Usman, A. Hanif, I.-H. Kim, and H.-J. Jung. Experimental validation of a novel piezoelectric energy harvesting system employing wake galloping phenomenon for a broad wind spectrum. *Energy*, 153, 06 2018.

[61] W. Wang, J. Cao, Y. Cai, S. Zhou, and J. Lin. Efficient energy harvesting from human motion by tristable piezoelectric cantilever. In *2015 Symposium on Piezoelectricity, Acoustic Waves, and Device Applications (SPAWDA)*, pages 14–17, 2015.

[62] M. Weigel, T. Lu, G. Bailly, A. Oulasvirta, C. Majidi, and J. Steimle. Iskin: flexible, stretchable and visually customizable on-body touch sensors for mobile computing. In *Proceedings of the 33rd Annual ACM Conference on Human Factors in Computing Systems*, pages 2991–3000, 2015.

[63] H. Wong and Z. Dahari. Human body parts heat energy harvesting using thermoelectric module. In *2015 IEEE Conference on Energy Conversion (CENCON)*, pages 211–214, 2015.

[64] L. YAN, J. YOO, B. KIM, and H.-J. YOO. A 0.5-μvrms 12-μw wirelessly powered patch-type healthcare sensor for wearable body sensor network. *IEEE journal of solid-state circuits*, 45(11):2356–2365, 2010.

[65] S. Yin, M. Kim, D. Kadetotad, Y. Liu, C. Bae, S. J. Kim, Y. Cao, and J.-s. Seo. A 1.06 μw smart ecg processor in 65 nm cmos for real-time biometrie authentication and personal cardiac monitoring. In *31st Symposium on VLSI Circuits, VLSI Circuits 2017*, pages C102–C103, 2017.

[66] T. Yoo, J. E. Kim, N. Le Ba, K.-H. Baek, T. T. Kim, et al. A 137-μw area-efficient real-time gesture recognition system for smart wearable devices. In *IEEE A-SSCC*, pages 277–280, 2018.

[67] X. Zhang, Z. Zhang, Y. Li, C. Liu, Y. X. Guo, and Y. Lian. A 2.89 μ w dry-electrode enabled clockless wireless ecg soc for wearable applications. *IEEE Journal of Solid-State Circuits*, 51(10):2287–2298, Oct 2016.

[68] X. Zhang, Z. Zhang, Y. Li, C. Liu, Y. X. Guo, and Y. Lian. A 2.89μw dry-electrode enabled clockless wireless ecg soc for wearable applications. *IEEE journal of solid-state circuits*, 51(10):2287–2298, 2016.

APPENDIX A

EXPERIMENTAL SETUP

This chapter provides detailed description of the experimental setup design, programming the controller and digital servo motor, and example waveforms to prove goodness of the setup.

A.1 CAD Model of Experimental Setup

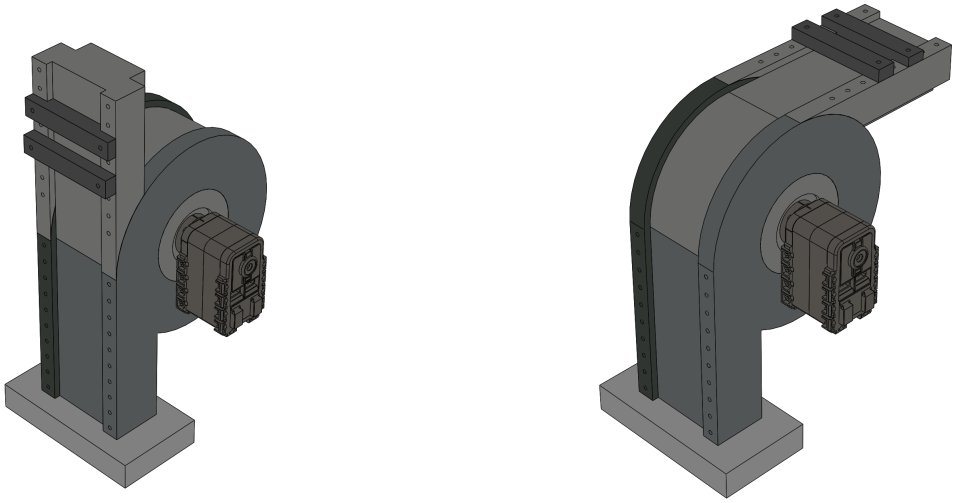

Figure A.1: CAD model of the new experimental setup which replicates human knee.

A.2 Programming OpenCM 9.04 and Dynamixel AX-12A

OpenCM9.04 is an Open-Source 32bit ARM Cortex-M3 based microcontroller board. It was chosen due to its compatibility with Arduino IDE, and hence the access to broad community support and native support for the Robotis Dynamixel servo motor family. To replicate the function of the controller used in this work, the following are crucial.

- Windows PC with Arduino IDE installed (https://www.arduino.cc/)
- OpenCM Board files (https://raw.githubusercontent.com/ROBOTIS-GIT/OpenCM9.04/master/arduino/opencm_release/package_opencm9.04_index.json)
- Dynamixel2Arduino.h library for Arduino IDE (Github: https://github.com/ROBOTIS-GIT/Dynamixel2Arduino)

Dynamixel AX-12A is a digital programmable servo motor by ROBOTIS. Key features include a 1Mbps TTL half-duplex asynchronous serial communication, 0° - 300° position control with a 0.29° step size (10-bit, 1023 levels), programmable torque and speed.

Programming the OpenCM to control the servo motor:

- Serial Port: Serial3, baud rate = 1M, DXL_PROTOCOL_VERSION$\bar{1}$.0
- Create a sine table containing only one cycle as follows :

sineTable[n] = round(512 + scaleFactor * (1+sin(2 * 3.14 * freq * (n * 0.01))) * (angle/2));

Where, scaleFactor = 3.4067

- At every 10 ms interval, update motor position with the next value in the sine table.

A.3 Verification with ADS

As repeatable, reproducible, and accurate measurements are crucial for analysis and concluding, the new experimental setup's movement accuracy was verified using a flexible angular displacement sensor (ADS). The ADS was first calibrated and then placed on the experimental setup. Bending angle data were obtained and analyzed for goodness. The measurements always remained within $\pm 2^{\circ}$ of the angle expected. Furthermore, the mathematical model used these angles as input. The following are the obtained waveforms from ADS.

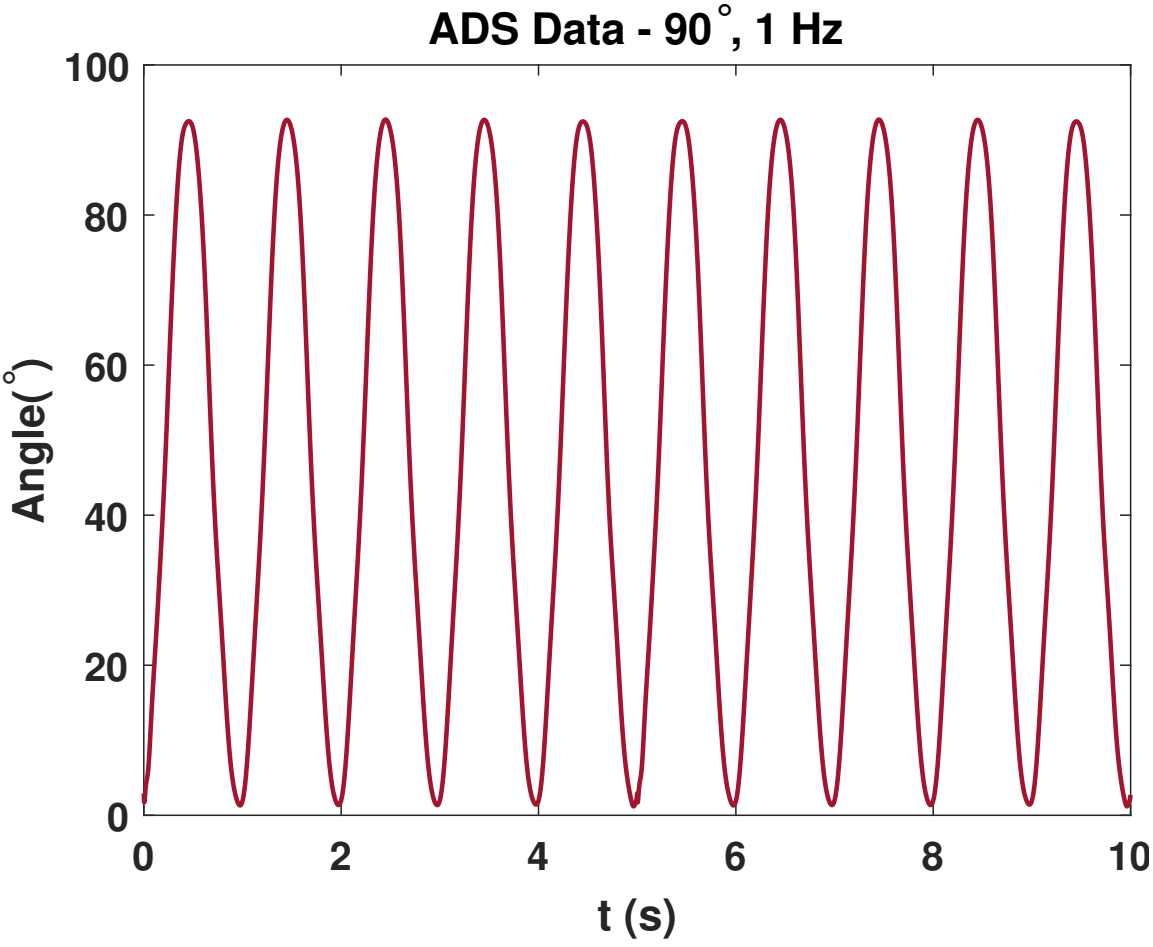

Figure A.2: Output of ADS for a 90° bending angle, 1 Hz excitation frequency.

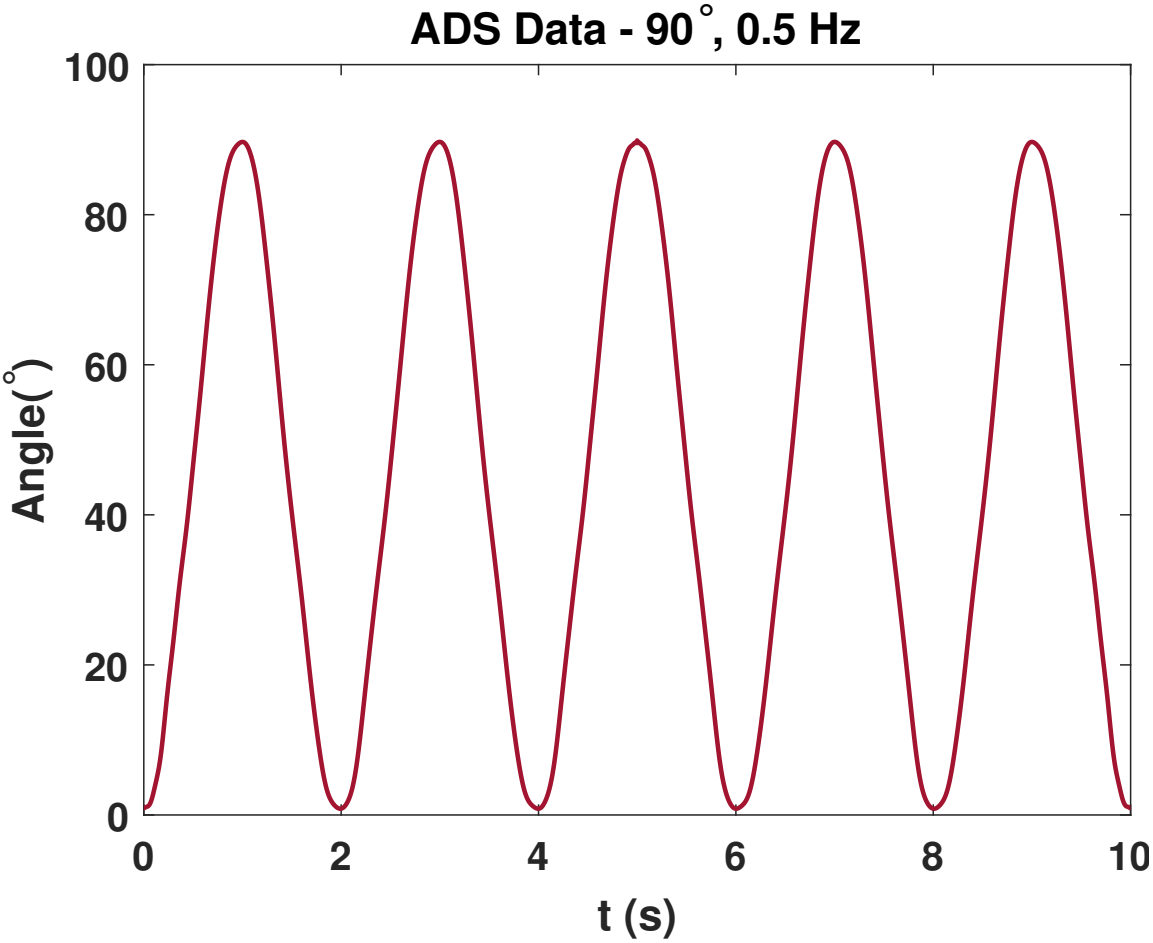

Figure A.3: Output of ADS for a 90° bending angle, 0.5 Hz excitation frequency.

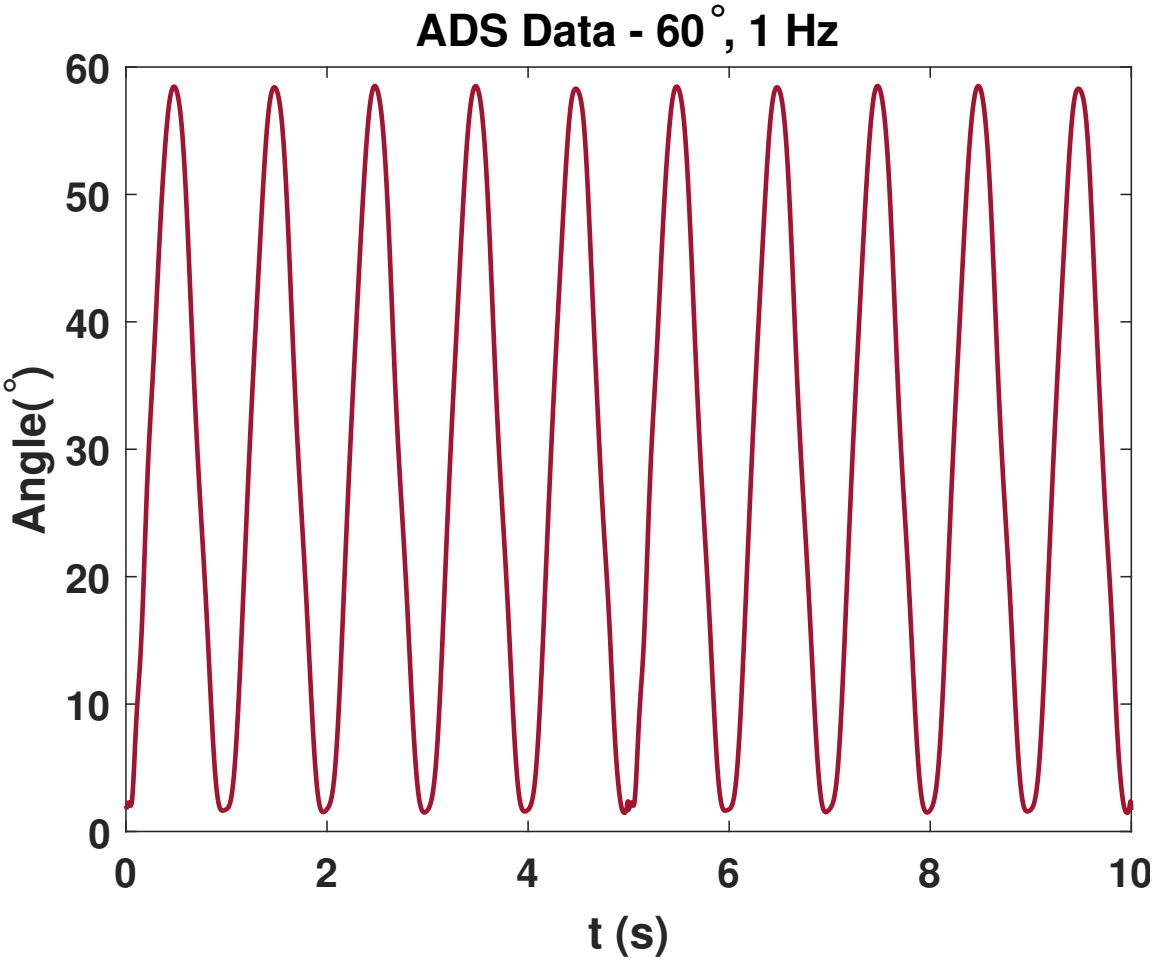

Figure A.4: Output of ADS for a 60° bending angle, 1 Hz excitation frequency.

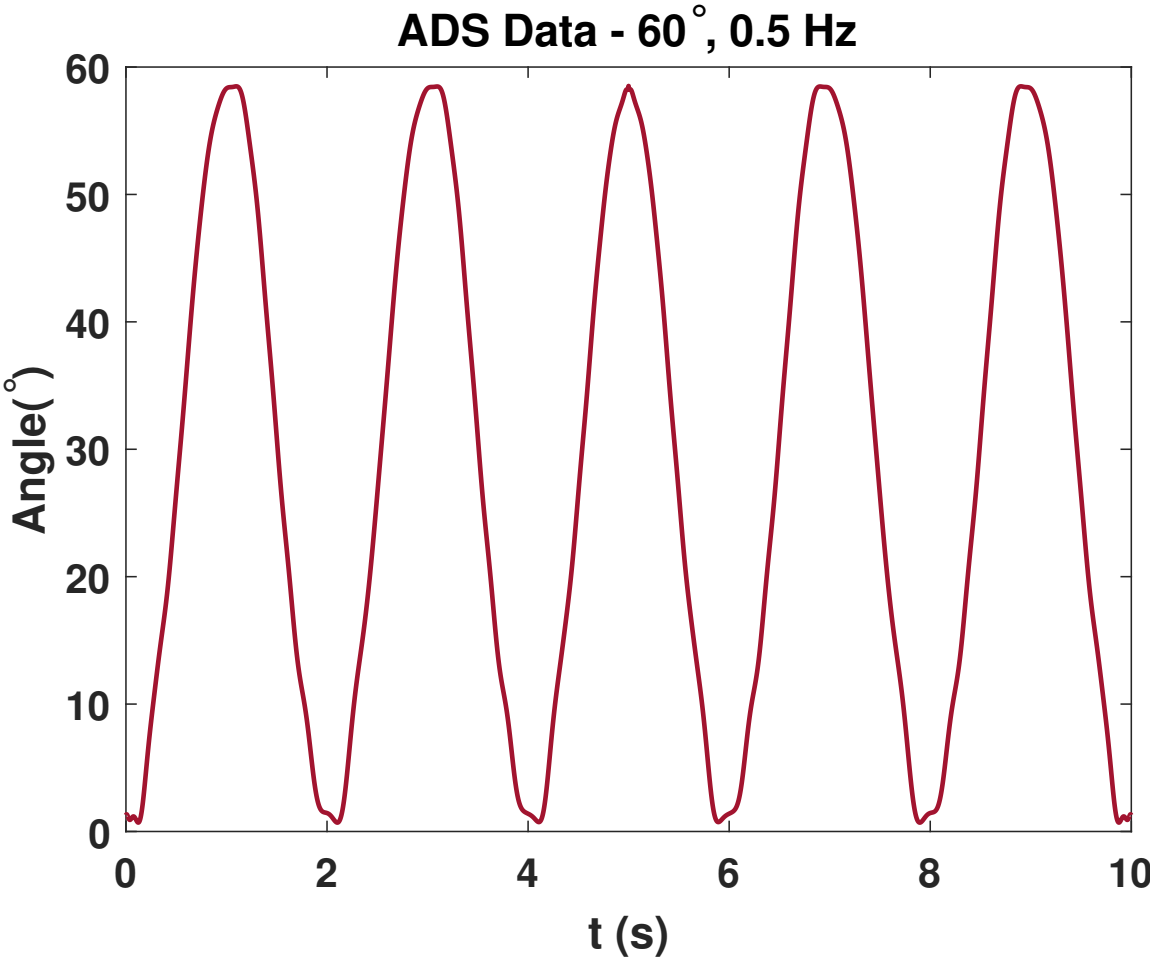

Figure A.5: Output of ADS for a 60° bending angle, 0.5 Hz excitation frequency.

APPENDIX B

EXPERIMENTAL DATA

This section shows experimental data obtained from the piezoelectric module MFC8514P2 and MFC8528P2.

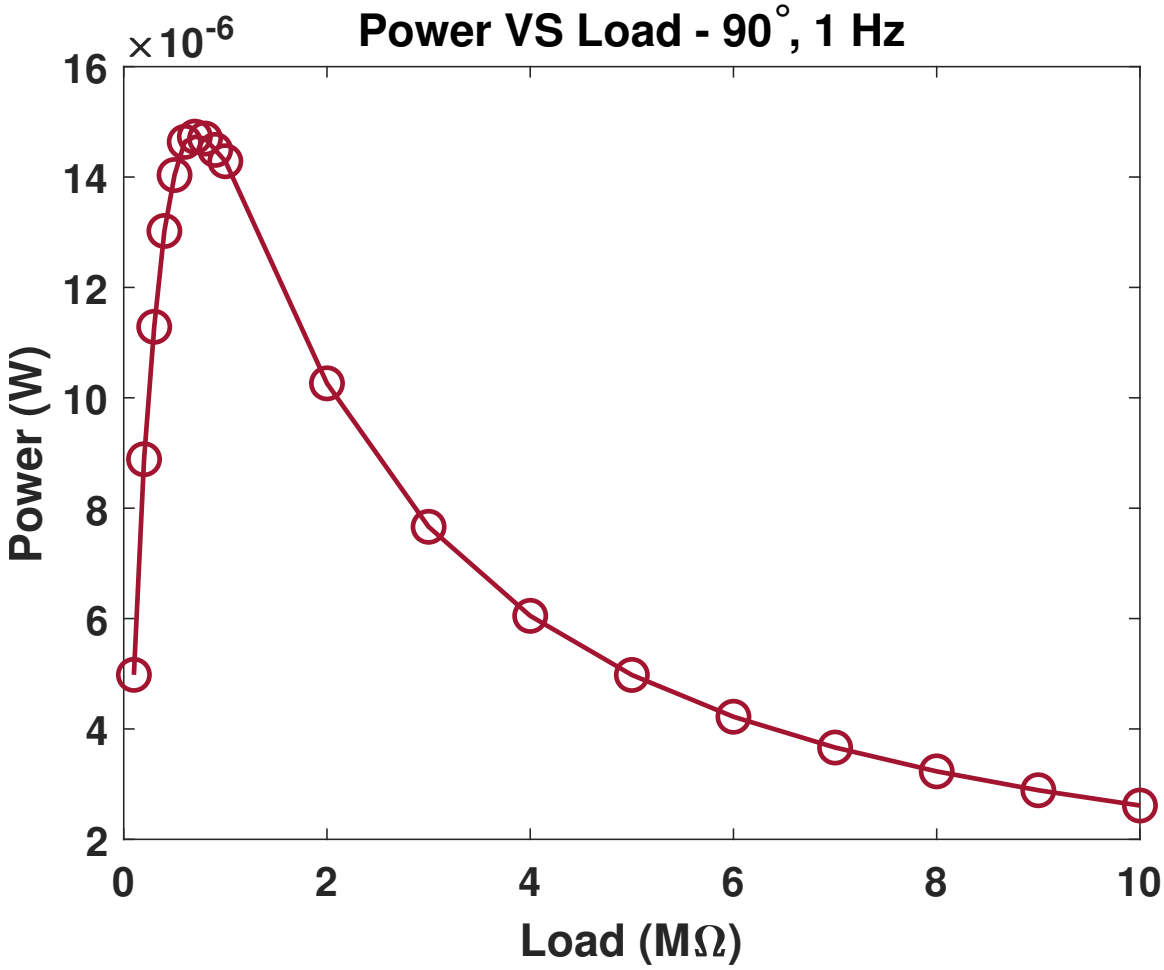

Figure B.1: Power plot of MFC8514P2. Input: 90° bending angle, 1 Hz excitation frequency. Load: R_{Load} = 0.1 MΩ - 10 MΩ

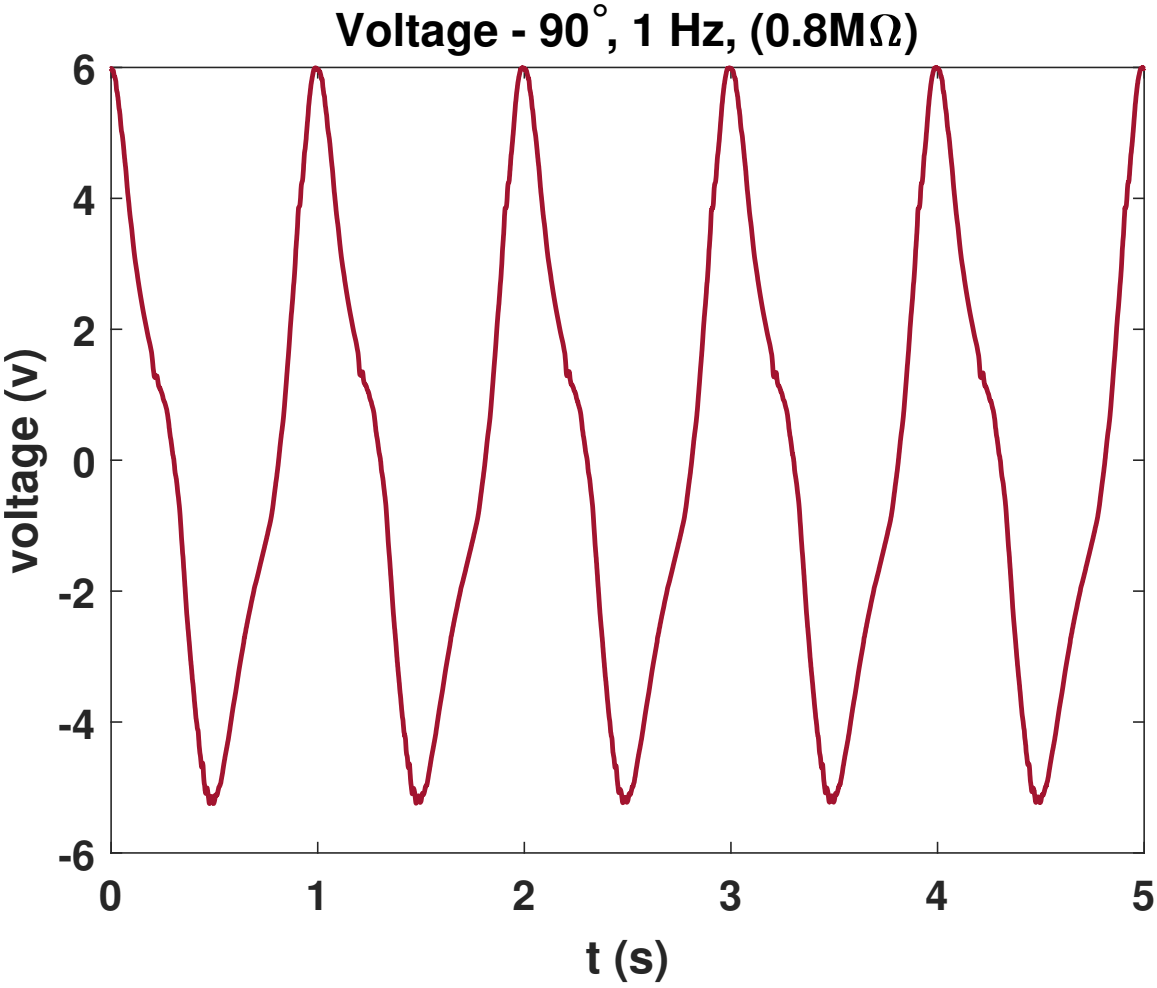

Figure B.2: Output of MFC8514P2. Input: 90° bending angle, 1 Hz excitation frequency. Load: R_{Load} = 0.8 MΩ

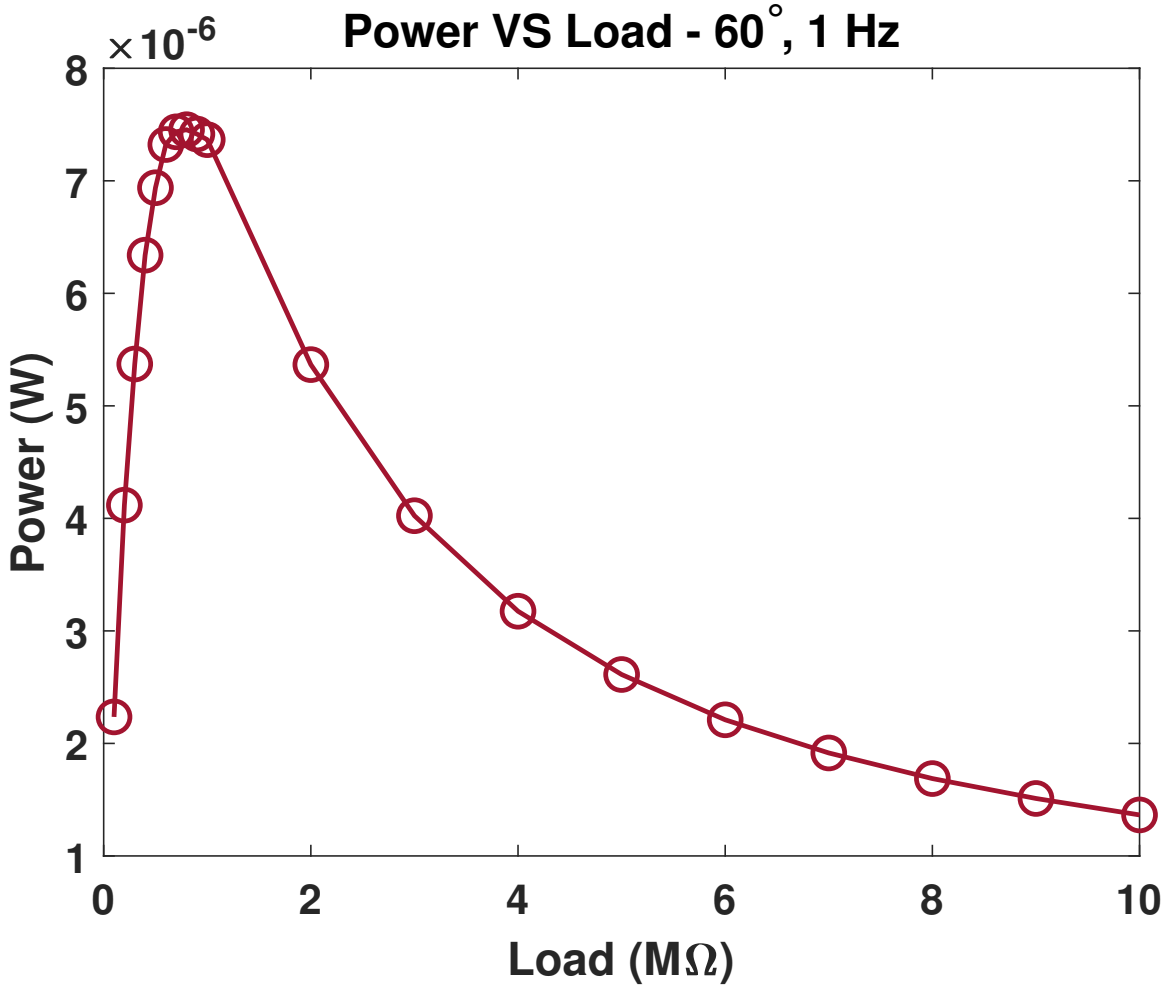

Figure B.3: Power plot of MFC8514P2. Input: 60° bending angle, 1 Hz excitation frequency. Load: R_{Load} = 0.1 MΩ - 10 MΩ

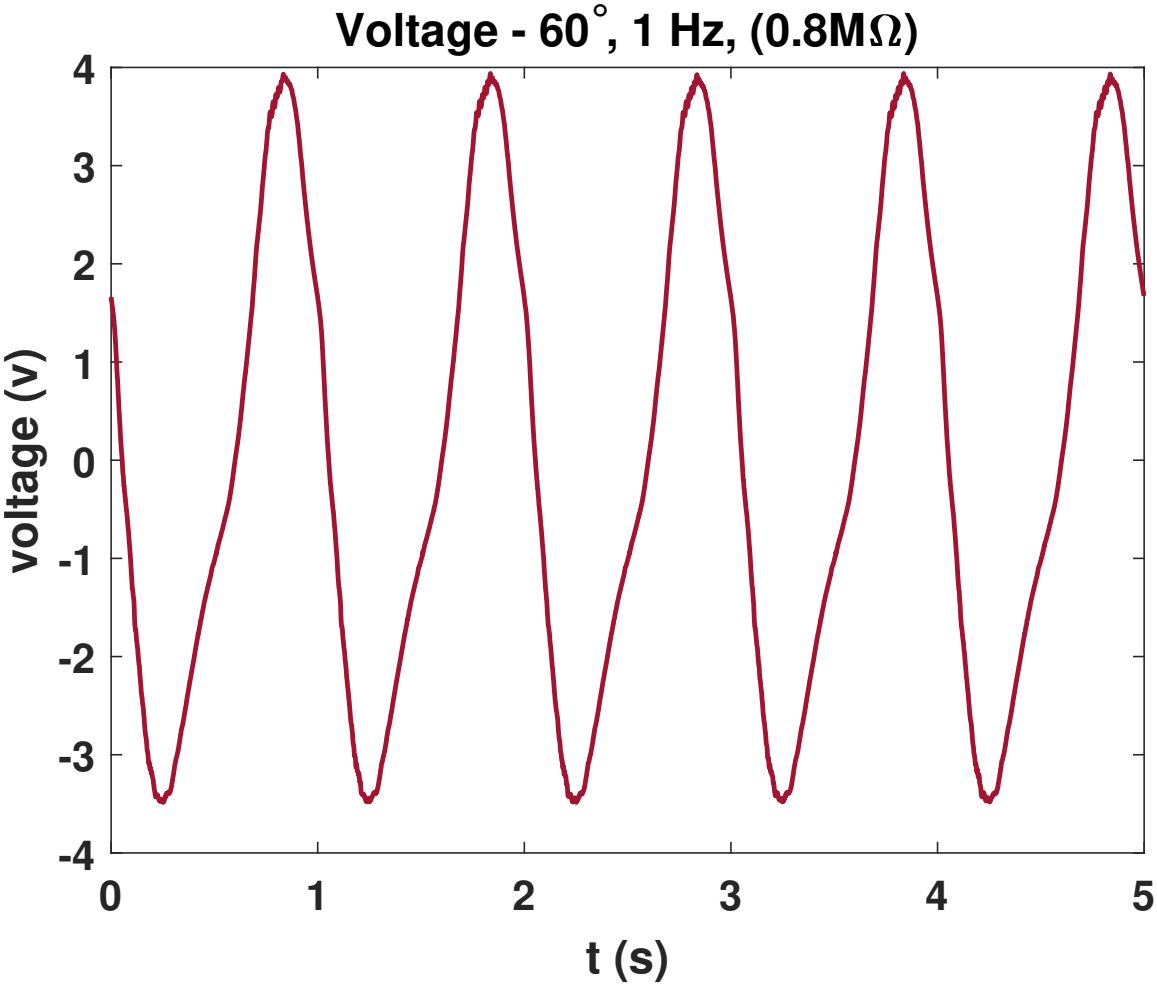

Figure B.4: Output of MFC8514P2. Input: 60° bending angle, 1 Hz excitation frequency. Load: R_{Load} = 0.8 MΩ

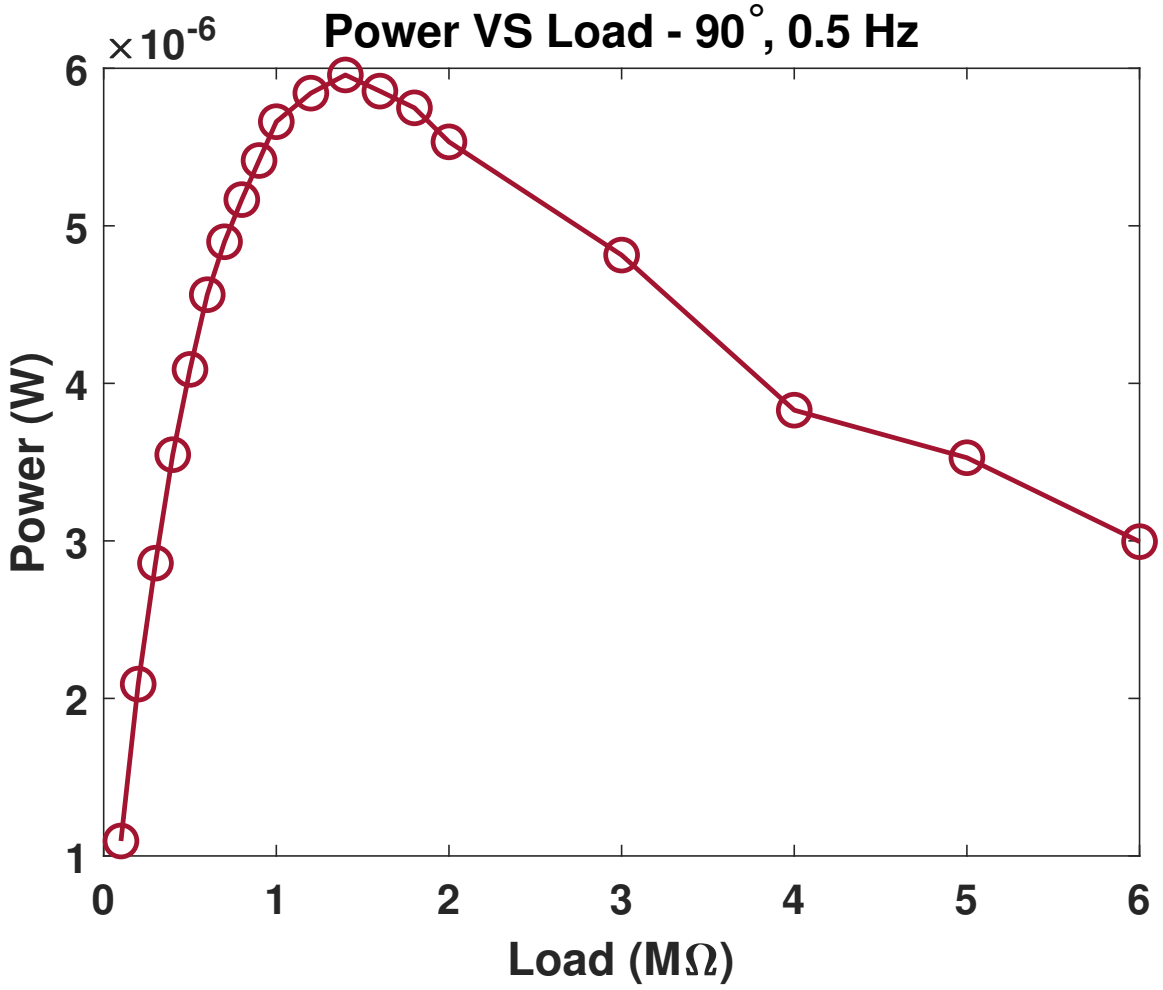

Figure B.5: Power plot of MFC8514P2. Input: 90° bending angle, 0.5 Hz excitation frequency. Load: R_{Load} = 0.1 MΩ - 6 MΩ

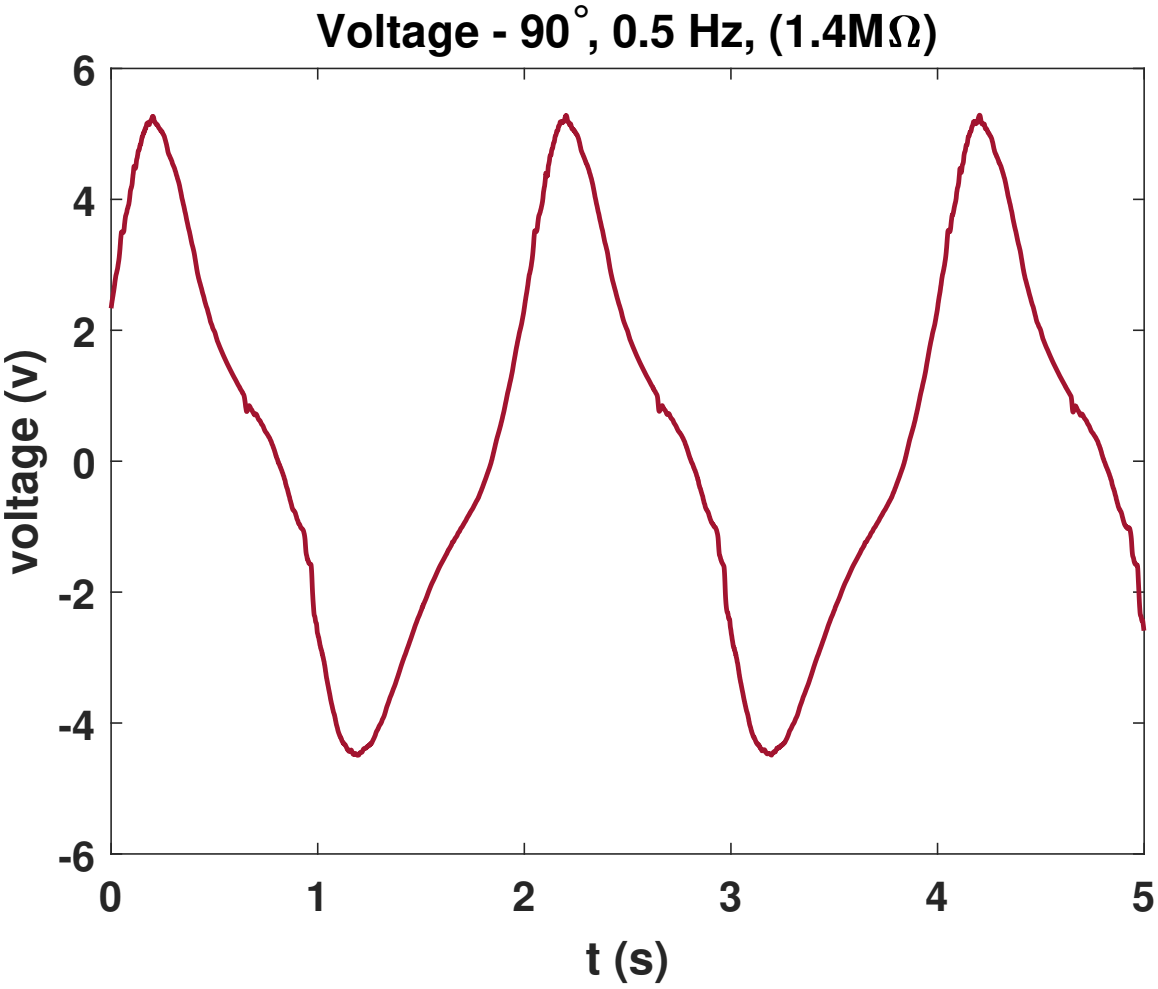

Figure B.6: Output of MFC8514P2. Input: 90° bending angle, 0.5 Hz excitation frequency. Load: R_{Load} = 1.4 MΩ

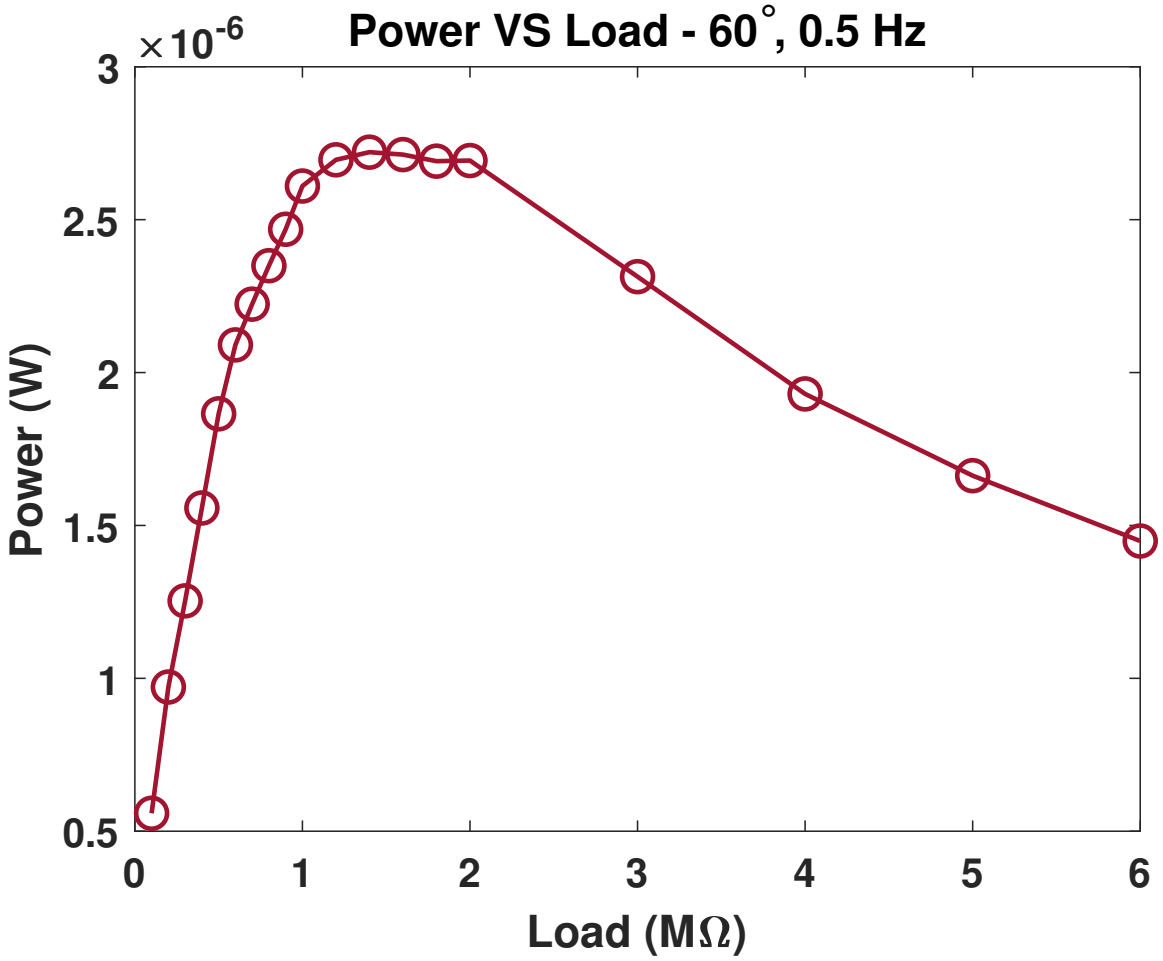

Figure B.7: Power plot of MFC8514P2. Input: 60° bending angle, 0.5 Hz excitation frequency. Load: R_{Load} = 0.1 MΩ - 6 MΩ

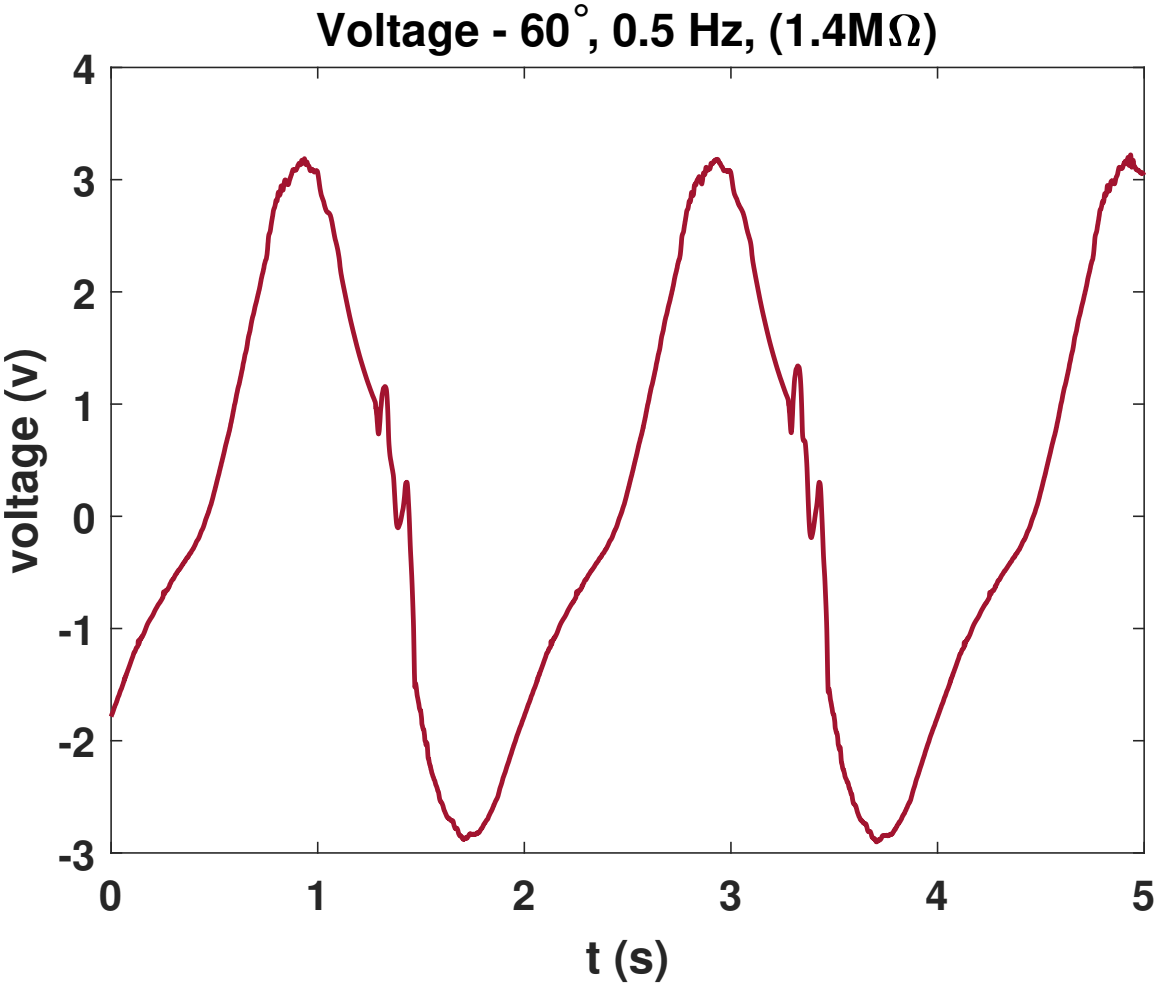

Figure B.8: Output of MFC8514P2. Input: 60° bending angle, 0.5 Hz excitation frequency. Load: R_{Load} = 1.4 MΩ

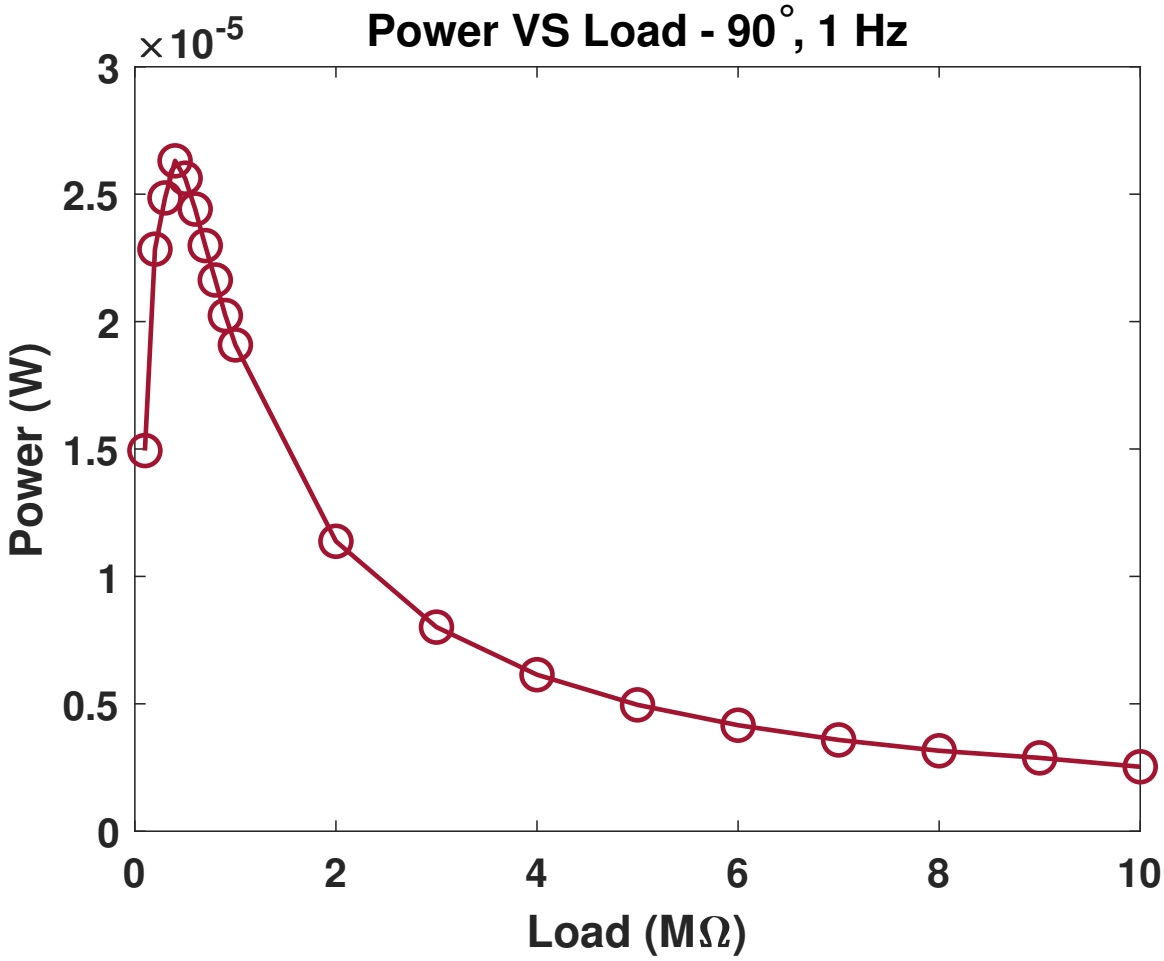

Figure B.9: Power plot of MFC8528P2. Input: 90° bending angle, 1 Hz excitation frequency. Load: R_{Load} = 0.1 MΩ - 10 MΩ

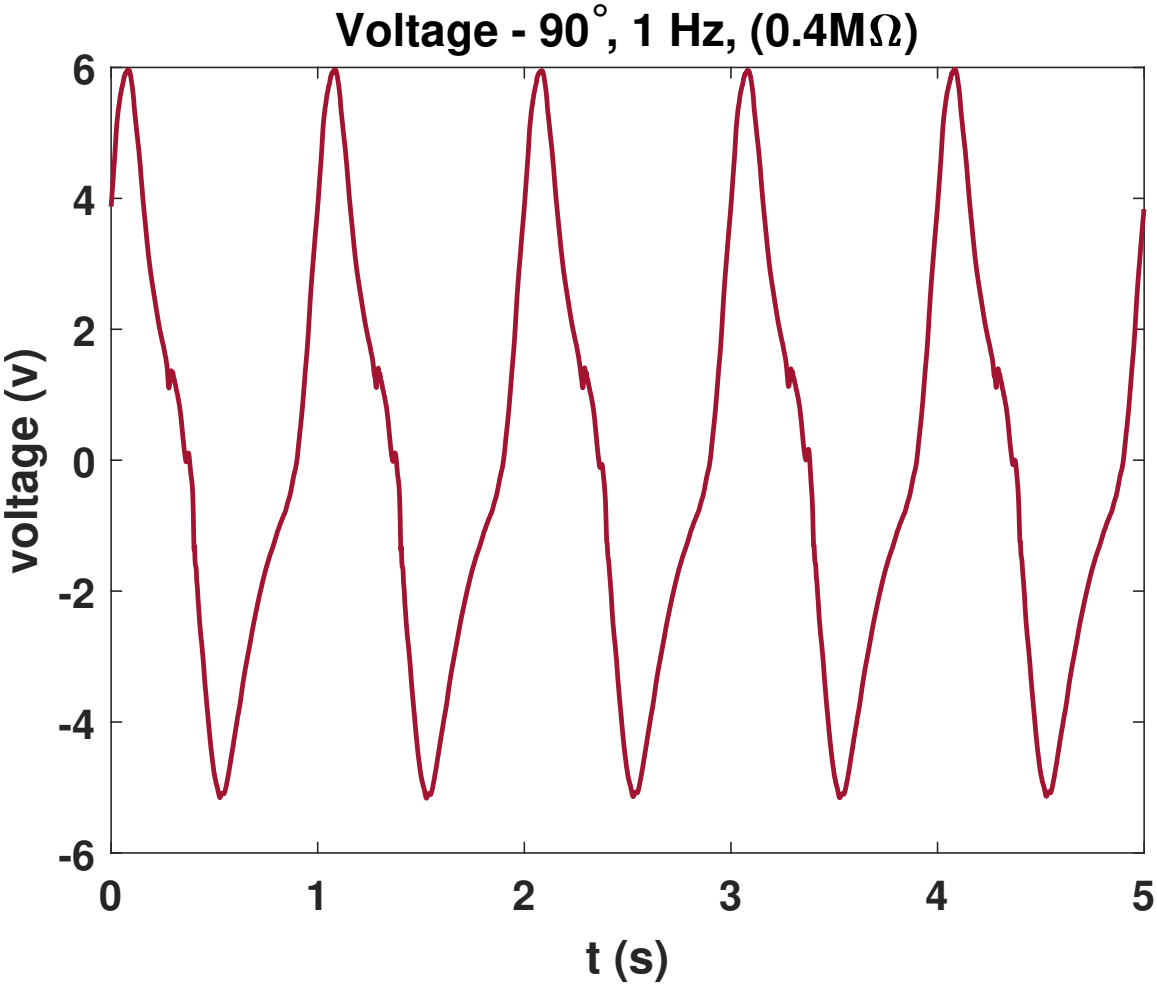

Figure B.10: Output of MFC8528P2. Input: 90° bending angle, 1 Hz excitation frequency. Load: R_{Load} = 0.4 MΩ

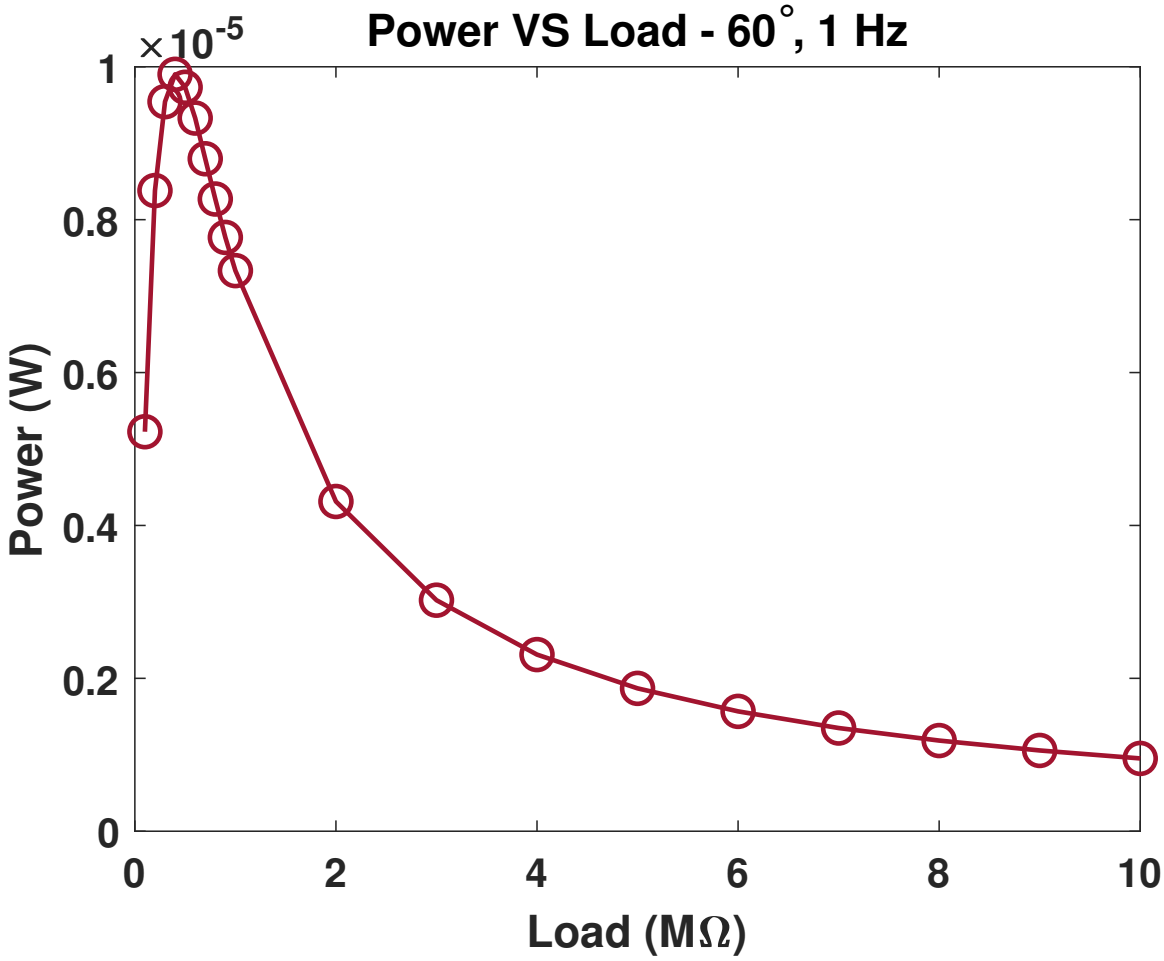

Figure B.11: Power plot of MFC8528P2. Input: 60° bending angle, 1 Hz excitation frequency. Load: R_{Load} = 0.1 MΩ - 10 MΩ

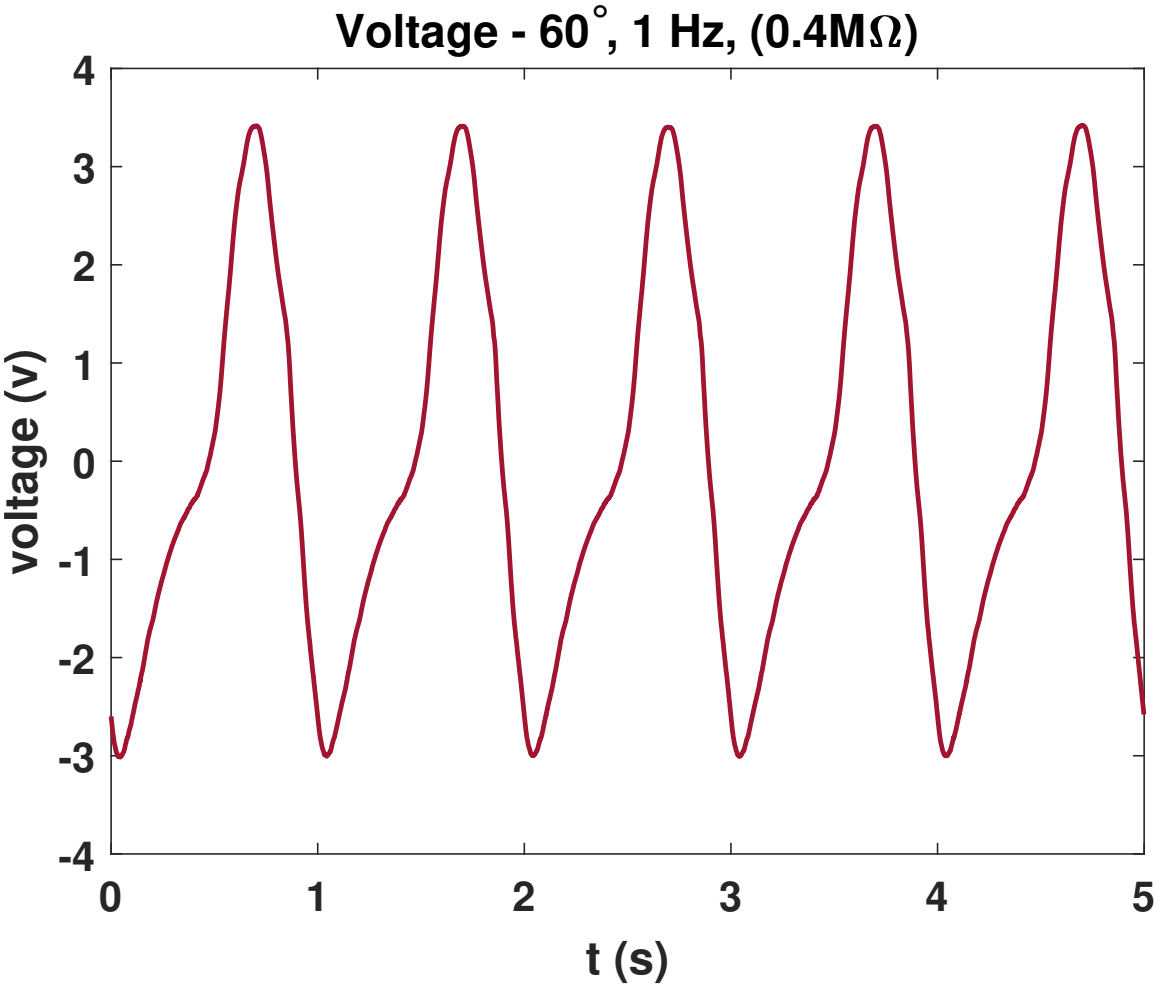

Figure B.12: Output of MFC8528P2. Input: 60° bending angle, 1 Hz excitation frequency. Load: R_{Load} = 0.4 MΩ

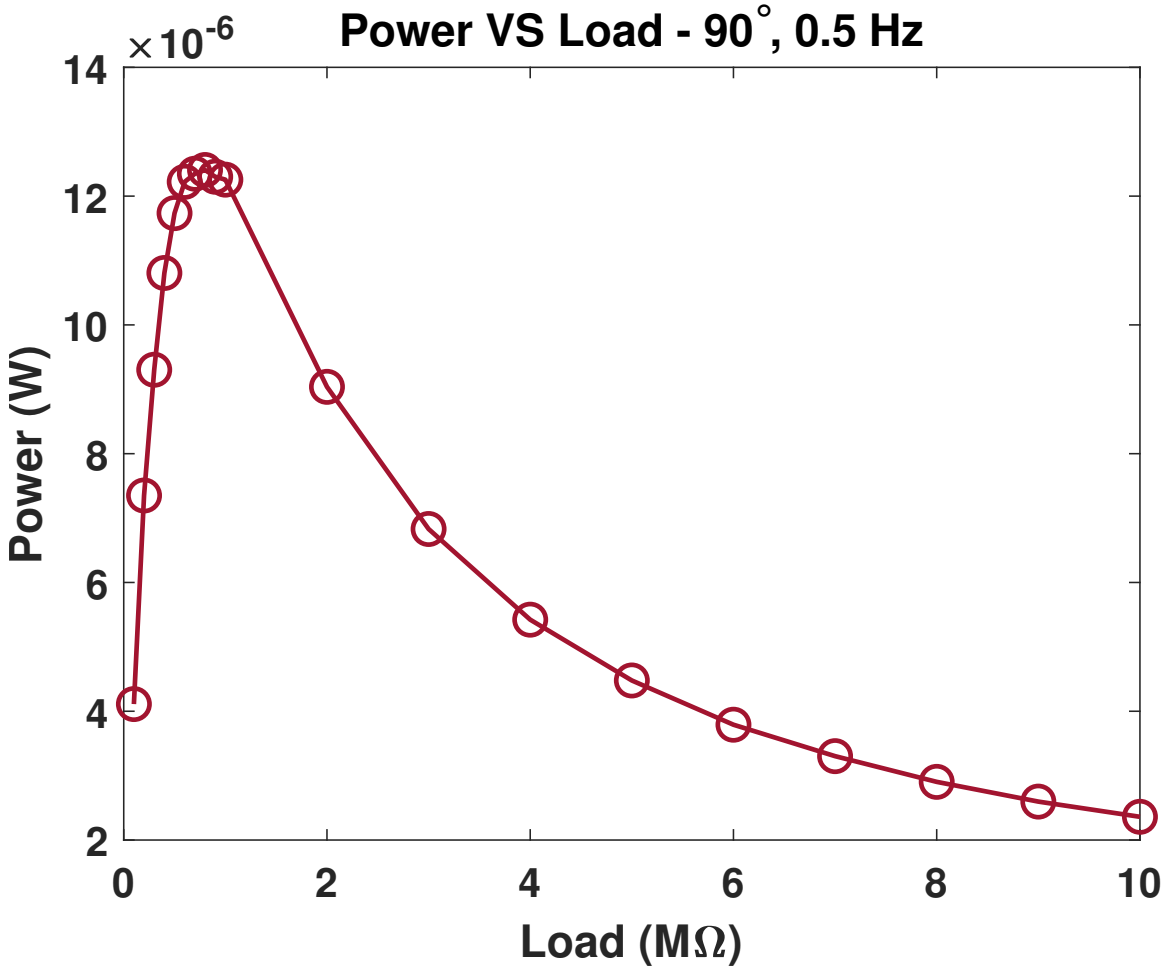

Figure B.13: Power plot of MFC8528P2. Input: 90° bending angle, 0.5 Hz excitation frequency. Load: R_{Load} = 0.1 MΩ - 10 MΩ

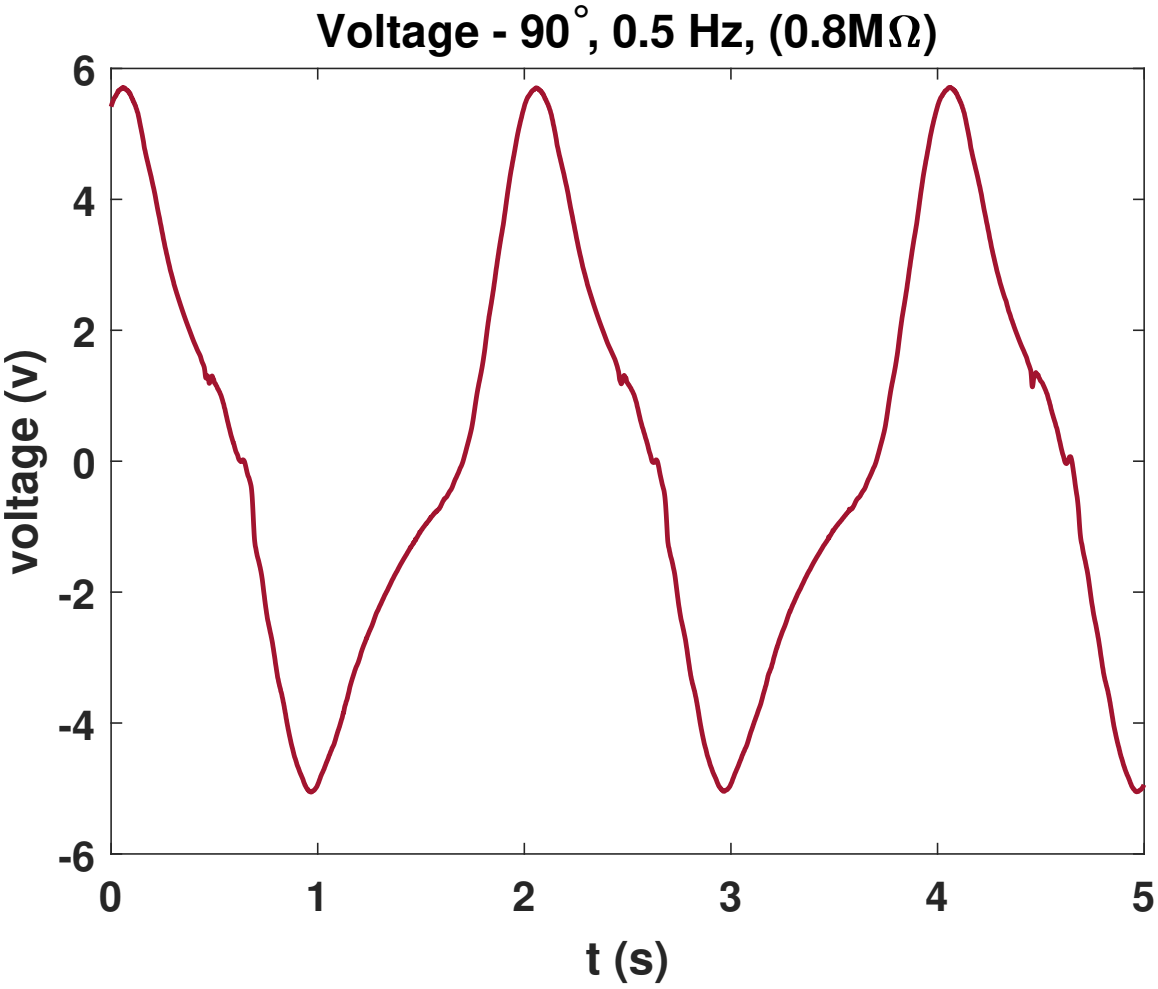

Figure B.14: Output of MFC8528P2. Input: 90° bending angle, 0.5 Hz excitation frequency. Load: R_{Load} = 0.8 MΩ

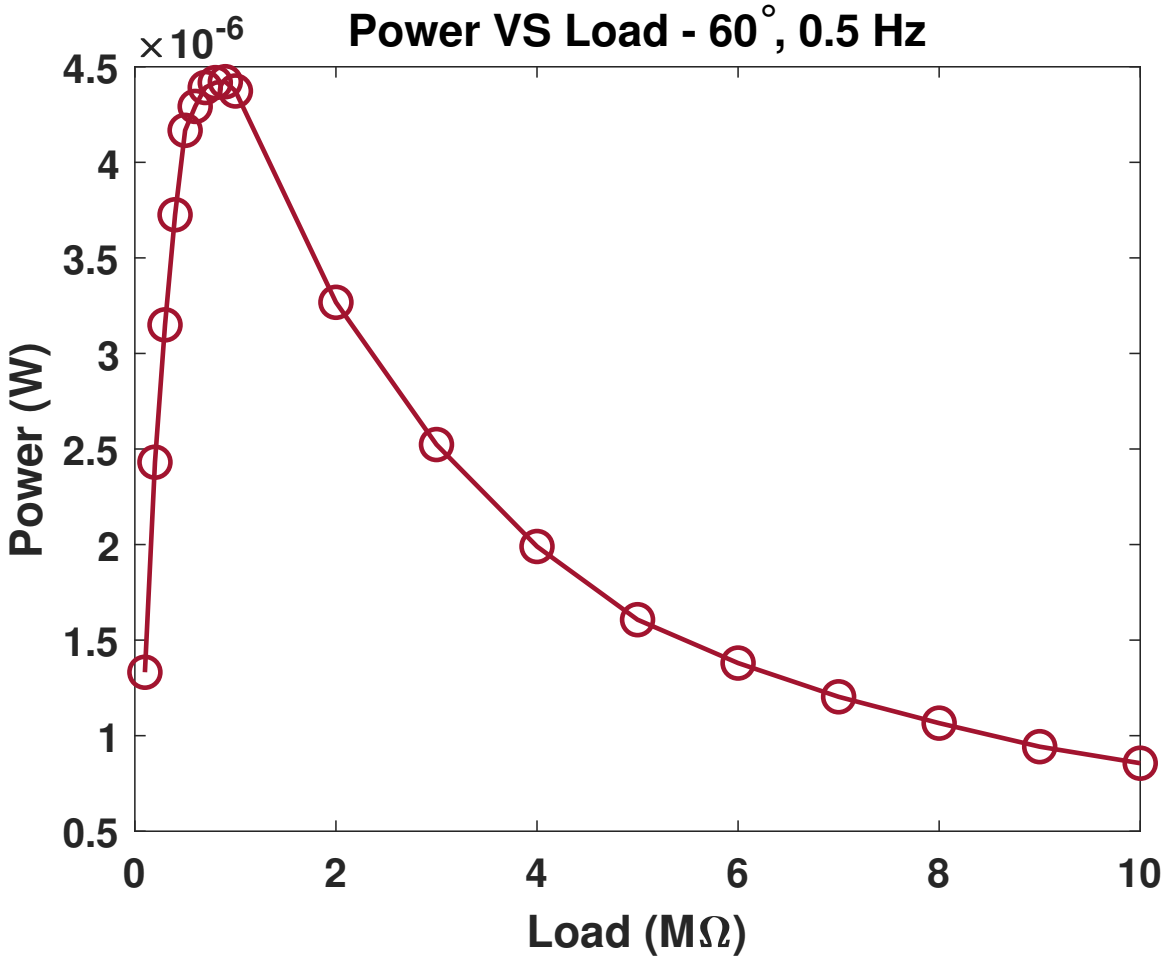

Figure B.15: Power plot of MFC8528P2. Input: 60° bending angle, 0.5 Hz excitation frequency. Load: R_{Load} = 0.1 MΩ - 10 MΩ

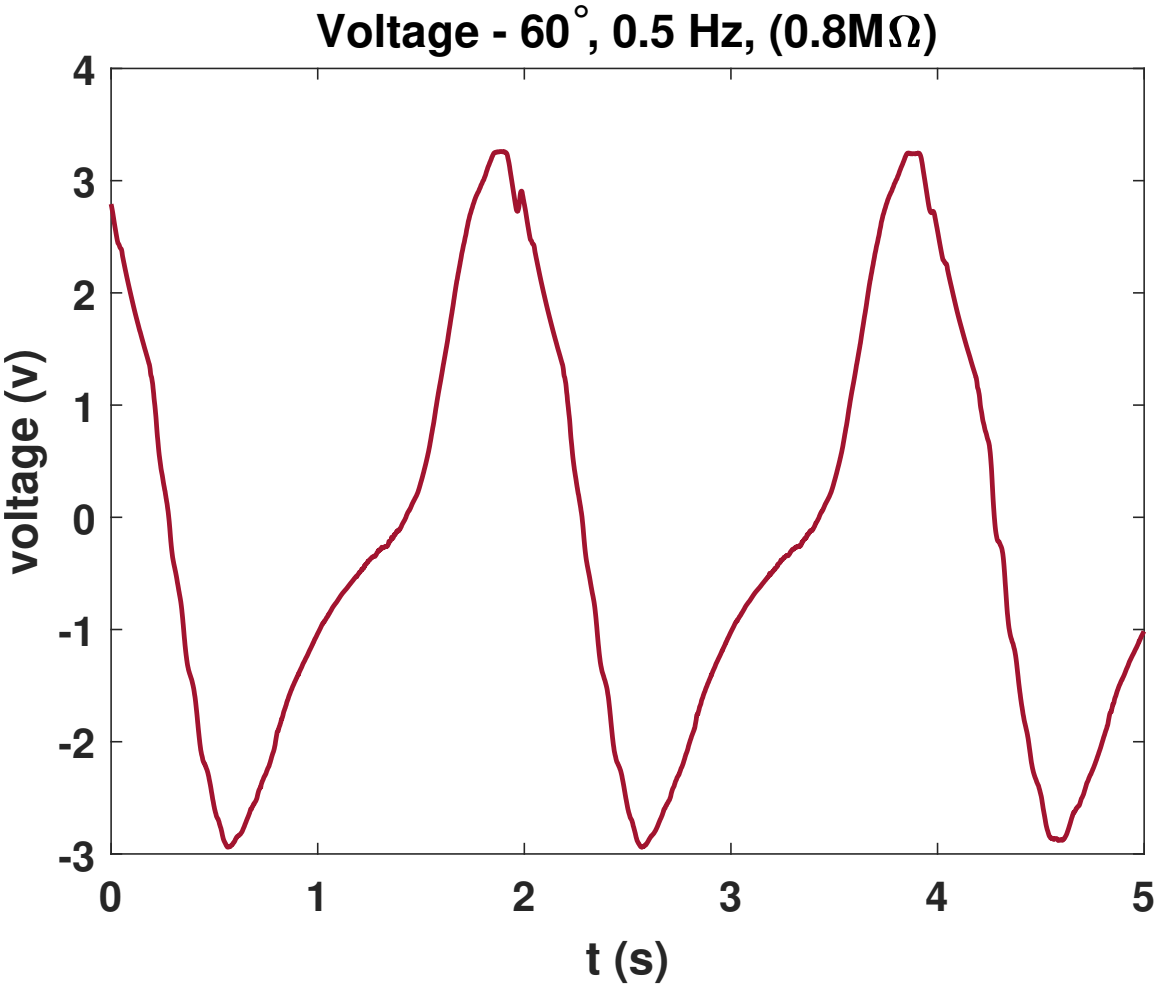

Figure B.16: Output of MFC8528P2. Input: 60° bending angle, 0.5 Hz excitation frequency. Load: R_{Load} = 0.8 MΩ